HR-STEM investigation of atomic lattice defects in different types of η precipitates in creep-age forming Al-Zn-Mg-Cu aluminium alloy

Tsai-Fu Chung[a], Yo-Lun Yang[b], Cheng-Ling Tai[a], Makoto Shiojiri[c], Chien-Nan Hsiao[d], Cheng-Si Tsao[a], Wei-Chih Li[e], Hsueh-Ren Chen[a], Zhusheng Shi[b], Jianguo Lin[b], Jer-Ren Yang[a,*]

[a] Department of Materials Science and Engineering, National Taiwan University, Taipei, Taiwan
[b] Department of Mechanical Engineering, Imperial College London, London SW7 2AZ, UK
[c] Kyoto Institute of Technology, Kyoto 606-8585, Japan
[d] National Applied Research Laboratories, Taiwan Instrument Research Institute, Hsinchu, Taiwan
[e] E.A. Fischione Instruments, Inc., 9003 Corporate Circle, Export, PA 15632, U.S.A.

*Corresponding author: Jer-Ren Yang

Tel: +886–2–33661314

Fax: +886–2–23634562

E-mail of Corresponding author: jryang@ntu.edu.tw

Graphical Abstract

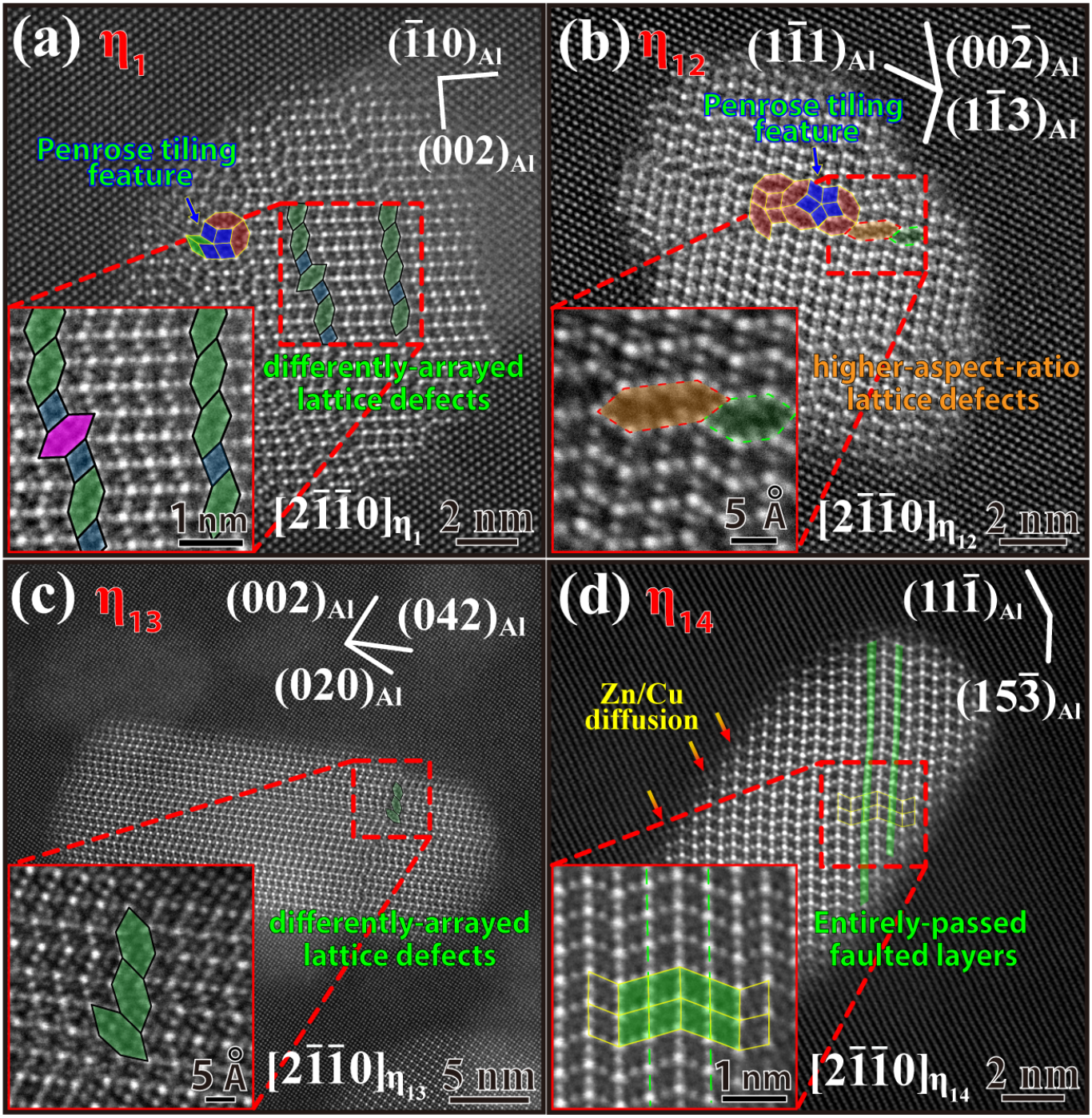

Highlights

1. Along the $[2\bar{1}\bar{1}0]\eta$ zone axis, the edge-on atomic configurations of η_1, η_2, η_{12}, η_{13} and η_{14} precipitates have been investigated to explore their atomic lattice defects.

2. Within the spherical-like morphologies of η_1 and η_{12}, Penrose tiling features jointed with elongated hexagonal lattice defects were identified.

3. In η_{12} precipitates, two types of elongated hexagonal lattice defects of different sizes were found.

4. Differently-oriented elongated hexagonal lattice defects presumably affect the local stackings, bringing about differently-oriented types of η precipitates.

5. In the newly-typed η_{14} precipitate, some entirely-passed stacking fault layers presumably cause a new specific orientation relationship with respect to the Al matrix.

Abstract

High-resolution (HR) high-angle annular dark-field (HAADF) scanning transmission electron microscopy (STEM) has revealed the atomic lattice defects in different types of η precipitates in the Al-Zn-Mg-Cu aluminium alloy subjected to creep-age forming treatment (with a constant stress lower than its room-temperature yield strength during ageing). Along the zone axes of $[110]_{Al}$ // $[2\bar{1}\bar{1}0]\eta$ of η_1 and η_{12}, $[112]_{Al}$ // $[2\bar{1}\bar{1}0]\eta$ of η_2 and $[100]_{Al}$ // $[2\bar{1}\bar{1}0]\eta$ of η_{13}, atomic projections of $(2\bar{1}\bar{1}0)\eta$ have been investigated. In those types of η, elongated hexagonal lattice defects (labelled as Type I defects) can be found; they are apparently related to local disorder in atomic stackings. Furthermore, in η_{12}, elongated hexagonal lattice defects with a much higher aspect ratio (labelled as Type II defects) are uniquely observed. These atomic lattice defects are presumably pertinent to the lattice accommodation in the course of creep-age forming. Additionally, in η_1 and η_{12}, the features of a Penrose tiling defect connecting with Type I defects are observed, and these complex defects obviously affect the growth direction of the precipitate, resulting in a nearly spherical morphology. Alternatively, several entirely-passed faulted layers in a new type of precipitate, η_{14}, consequently bring about a new orientation relationship: $(51\bar{3})_{Al}$ // $(0001)\eta_{14}$ and $[112]_{Al}$ // $[2\bar{1}\bar{1}0]\eta_{14}$. Moreover, in an atomic STEM image of η_{14}, the significant Z-contrast gradient adjacent to the transformation front of η_{14} elucidates the Zn/Cu diffusion from the matrix to the precipitate along $\{1\bar{1}\bar{1}\}_{Al}$ planes at the interface.

Keywords: Scanning transmission electron microscopy; Al-Zn-Mg-Cu aluminium alloy; Creep-age forming; Elongated hexagonal lattice defects; Atomic lattice defects

1. Introduction

It has been reported [1-3] that in Al-Zn-Mg-Cu aluminum alloys undergoing plastic deformation before and during aging treatment, dynamic precipitation is accompanied by many lattice defects in aluminium matrix, such as vacancies and dislocations, which are favorable nucleation sites for nanoprecipitation. Continuous generation of lattice defects in the matrix of aluminum alloys [1-3] can effectively enhance the solid-state precipitation, thereby conferring a higher strengthening effect than the traditional peak aging treatment. However, whether the atomic lattice defects interact with the precipitates and further change their atomic structures remains to be clearly studied. Recently, the creep-age forming (CAF) process, which maintains a constant-uniaxial elastic stress during ageing, has been applied to Al-Zn-Mg-Cu and Al-Cu-Li aluminium alloys for the production of aircraft wings [4-8]. In the works on Al-Zn-Mg-Cu aluminium alloys subjected to CAF [9-13], it is reported that the forming stress not only changes the distribution of precipitates [9, 10] but also increases the nucleation sites of precipitates [9-13]. Especially, it has been claimed that the diffusion rates of solute atoms and vacancies are significantly facilitated by the tensile stress during CAF, leading to a higher density of η precipitates than that resulting from compression during CAF [13]. Furthermore, increasing the level of tensile/compressive stress (i.e., that of tensile CAF from 200 MPa to 260 MPa [9, 12] and that of compressive CAF from 260 MPa to 340 MPa [13]) apparently creates more lattice defects in the aluminium matrix, which are effective channels for solute atoms to enhance the formation of η precipitates [13]. However, no investigations to date have clarified whether the induced

atomic lattice defects during CAF influence the transformation of η and lead to changes in the atomic stackings of η with new orientation relationships.

In the CAF samples of Al-Zn-Mg-Cu alloys, the precipitate sequence of GP zones → η' precipitates → η precipitates still can be observed [10, 14-16]. The η precipitates have been determined to have a hexagonal (HCP) structure with a space group $P6_3/mmc$ [15, 17-20]. The typical stochiometric η-$MgZn_2$ is known to possess one of the stacking characteristics of Laves phases, C14 [21-23]. Fourteen different types of η precipitates and their corresponding orientation relationships have been reported in previous investigations [15, 17-19, 24]. High-resolution (HR) high-angle annular dark-field (HAADF) scanning transmission electron microscopy (STEM), which has become popular in the investigation of nanometer-sized precipitates, has provided new insights into the identification of η [16, 19, 24-29]. On the two-dimensional (2-D) projection plane of $(2\bar{1}\bar{1}0)\eta$, η_1 and η_2 precipitates generally possess the zig-zag C14 ($\cdots RR^{-1}RR^{-1}\cdots$) atomic configurations, where R units represent the projected rhombic-units, and R^{-1} units, the inversely projected rhombic-units, based on the structural model proposed by Marioara et al. [25]. However, η_1 and η_2 precipitates have been found to contain some elongated hexagonal lattice defects with different orientations [16, 24, 27-29]. Those works [16, 24, 27-29] have reported that under observation along the $[2\bar{1}\bar{1}0]\eta$ // $[110]_{Al}$ zone axis, the differently-oriented elongated hexagons in η_1 and η_2 are extremely similar to the sub-structure of β_1' (Mg_4Zn_7) in the Mg-based alloys [30, 31], which consists of 6 differently-oriented pairs of rhombic units, enveloped by 2 differently-oriented pairs of an elongated hexagonal unit

interwoven with a rhombic unit. However, the complete atomic structure of β_1'-Mg_4Zn_7 [16, 24, 27-29] has not been found on the atomic projection $(2\bar{1}\bar{1}0)\eta$ plane of η_1 and η_2 in aluminium-based alloys.

Alternatively, in the previous works on the Al-Zn-Mg(-Cu) aluminium alloys aged at 120 °C for 167 h [28] and for 568 h [29], the number of the elongated hexagonal lattice defects were found to be favourably associated with the faulted layer between the repeated rhombic units in η_1 [28] and η_2 [29]. In the former work [28] on the $(2\bar{1}\bar{1}0)\eta$ configurations of η_1, the regular zig-zag stacking $\cdots RR^{-1}RR^{-1}\cdots$, which was inserted the same rhombic unit (R or R^{-1}) as the front unit, were found to become $\cdots RR^{-1}R^{\downarrow}_{\uparrow}RR^{-1}\cdots$ or $\cdots RR^{-1}{}^{\downarrow}_{\uparrow}R^{-1}RR^{-1}\cdots$ stackings (the double arrows indicate the faulted layer). In the latter work [29], it was found that the $(2\bar{1}\bar{1}0)\eta$ atomic projections of η_2 precipitates frequently have not only two repeated rhombic units (i.e., $R^{\downarrow}_{\uparrow}R$ or $R^{-1}{}^{\downarrow}_{\uparrow}R^{-1}$), but also three repeated rhombic units (i.e., $R^{\downarrow}_{\uparrow}R^{\downarrow}_{\uparrow}R$ or $R^{-1}{}^{\downarrow}_{\uparrow}R^{-1}{}^{\downarrow}_{\uparrow}R^{-1}$). Although these previous investigations [28, 29] have displayed the 2-D atomic arrays accompanied by lattice defects in η precipitates, the related 3-D reconstructed structure of η precipitates has not yet been reported. Regarding this aspect, the present work attempts to employ the six Komura units (A, B, C, A', B' and C') [21] to construct the 3-D structure of η-$MgZn_2$ Laves phases. Moreover, it has been reported that three shortest stacking sequences of Laves phases, AB', ABC and AB'A'C, [21] are generally named as C14, C15, and C36 structures, respectively [21, 23, 32-40]. Under the observation of the $[2\bar{1}\bar{1}0]$ zone axis of η_2 precipitates [16, 25, 29], the zig-zag rhombic configuration ($\cdots RR^{-1}\cdots$) on the 2-D atomic image has been employed to fit the stackings of the C14 structure in the 3-D structure. Additionally, on the atomic projection $(2\bar{1}\bar{1}0)$ planes of η_1 [28] and η_2 [29], two and three repeated rhombic layers (i.e.,

$\cdots R\underline{R^{-1}R^{-1}}R\cdots$ and $\cdots\underline{RRR}\cdots$) embedded in the zig-zag rhombic arrangements were claimed to be the stackings of C36 and C15, respectively. However, Komura stackings of AB'A'C and ABC were not reported in those works [28, 29]. In Supplementary Fig. 1 in Supplementary Material, the schematic diagrams show 2-D atomic projections of $(2\bar{1}\bar{1}0)\eta$ for C36 and C15 with respect to that of C14. The C36 structure is assembled by AB'A'C stacking with a sketch of 2-D rhombic units $\cdots RR^{-1}R^{-1}R\cdots$; the C15 structure, by ABC stacking with a sketch of 2-D rhombic units $\cdots RRR\cdots$. Here, it is hard to distinguish the differences among 2-D repeated rhombic units such as the R^{-1} units in $R^{-1}R^{-1}$ stacking, the R units in RR stacking of C36, and the R units in RRR stacking of C15. However, for the 3-D atomic structure of η, which is built up by Komura model [21], the $R^{-1}R^{-1}$ and RR of C36 on the projection plane $(2\bar{1}\bar{1}0)\eta$ can be identified by B'A' and CA, respectively, whereas the RRR stackings of C15 can be regarded as ABC. The observation of the repeated rhombic layers in the different η precipitates, which exhibit the same 2-D atomic projection as pointed out in the above cases, is easily misleading.

In the present work, by employing HAADF STEM along the $[110]_{Al}$, $[100]_{Al}$ and $[112]_{Al}$ zone axes, it is assumed that the zig-zag rhombic configuration of η_1, η_2, η_{12} and η_{13} precipitates on the $(2\bar{1}\bar{1}0)\eta$ projection plane are based on the C14 (AB') stackings. During CAF, the atomic lattice defects and layered faults, which form within those of η, are suggested to be associated with the changes in stackings, which can be examined by the six Komura units (A, B, C, A', B' and C') of η [21]. Accidently, a new crystallographic orientation between the η-precipitate and the aluminium matrix was found in the present work, and this new type of precipitate is designated as η_{14}. The Z-contrast

image at the transformation front of η_{14} has been investigated to reveal the traces of the diffusion of solute atoms.

2. Materials and methods

The chemical composition of the AA7050 aluminium alloy investigated in the present work is Al-6.25Zn-2.14Mg-2.23Cu-0.05Fe-0.03Si (wt.%). After solution treatment at 475°C for 1 h with water quenching to room temperature, the samples were treated by three-step ageing: (i) at 120°C for 8 h, (ii) at 165°C for 1 h, and (iii) at 174°C respectively for 2, 4, 6, and 8 h. During the third step of ageing, an applied constant tensile stress of 162.5 MPa was loaded on the samples to induce creep. This step of the ageing was the so-called creep-age forming (CAF), so the resulting samples are referred to as CAF samples.

The mechanical strength, the ultimate tensile strength (σ_{UTS}) and the yield strength (σ_{yield}) of the pure-aged (without the applied constant creep forming stress of 162.5 MPa in the third step) and creep-aged (with the creep forming stress of 162.5 MPa in the third step) specimens were measured on the Instron 5584 system at a strain rate of 10^{-4} s^{-1}. The Vickers Hardness tests were performed with a Future-Tech Fm-700 hardness testing machine on the pure-aged samples and different CAF-aged samples, those treated for 2, 4, 6, and 8 h in the third step. The value of hardness was measured by forcing the Vickers indenter into the surface of the prepared samples at a load of 1000 gf. The load application time for one indentation was 10 s, and the average hardness value for each specimen was determined from 30 tests on the corresponding sample.

TEM/STEM specimens were prepared by cutting discs from the CAF samples treated for 8 h and thinning them to 0.07 mm thickness before they were twin-jet electropolished in a mixture of 33% nitric acid and 67% methanol at -20 °C with a working voltage of 11 V. Then an M1040 NanoMill TEM specimen preparation system (E.A. Fischione Instruments) and an M1070 Nanoclean plasma cleaner (E.A. Fischione Instruments) were subsequently employed so that the oxidation layers and the hydrocarbon contamination of the pre-observed TEM specimens could be assumed to be eliminated. Afterwards, HAADF-STEM observations were performed with an FEI Titan Chemi-STEM microscope equipped with a spherical aberration corrector (Cs-corrector) which achieves a ~0.1 nm probe size with a beam current of ~70 pA and a convergence semi-angle of ~19.8 mrad. Under the 135 nm camera length of the FEI Titan Chemi-STEM microscope, all HAADF STEM images were recorded with a HAADF detector with a collecting angle range of ~35.9 mrad (inner angle) to ~143.6 mrad (outer angle). The simulated atomic arrangement of the $(2\bar{1}\bar{1}0)\eta$ zig-zag array and the $(0001)\eta$ six-fold symmetric configuration were constructed with the Vienna *ab initio* simulation package (VASP) [41, 42] using the structural model of η (a space group of $P6_3/mmc$, and lattice constants of a = b = 0.522 nm and c = 0.856 nm) proposed by Marioara [25] and Wolverton et al. [43].

3. Results

3.1 Mechanical strength and precipitates of pure-aged and CAF-aged processes

Figs. 1a and 1b present the data of the ultimate tensile strength (σ_{UTS}), yield strength (σ_{yield}) and hardness (HV), respectively for the CAF samples and samples with the same ageing times (2, 4, 6 and 8 h) without stress. In Figs. 1c-f, the low-magnification STEM images of 8 h pure-aged and CAF-aged samples reveal η precipitates (indicated by red arrows) in the aluminium matrix. It should be noted that under STEM observation, the precipitates appear with white contrast, whereas the dark-imaging particles are due to the removal of the precipitates during the TEM/STEM sample preparation. The higher number of dislocations (indicated by green arrows) in the CAF aged samples (Fig. 1f) with respect to the pure aged samples (Fig. 1d) indicates the higher possibility of the interaction between precipitates and dislocations, where the impingement between η phases and the tangled dislocations would occur during CAF. The concurrent dynamic precipitations and the transitions of η' and η precipitates during CAF have quantitatively been resolved from small angle X-ray scattering (SAXS). The SAXS result is illustrated in Supplementary Fig. 2 and Supplementary Table 1 in Supplementary Material. However, the resultant atomic structures of η due to the processing of CAF has yet to be clearly understood. Moreover, what kinds of atomic lattice defects are induced within η during CAF will be addressed in Section 3.3.

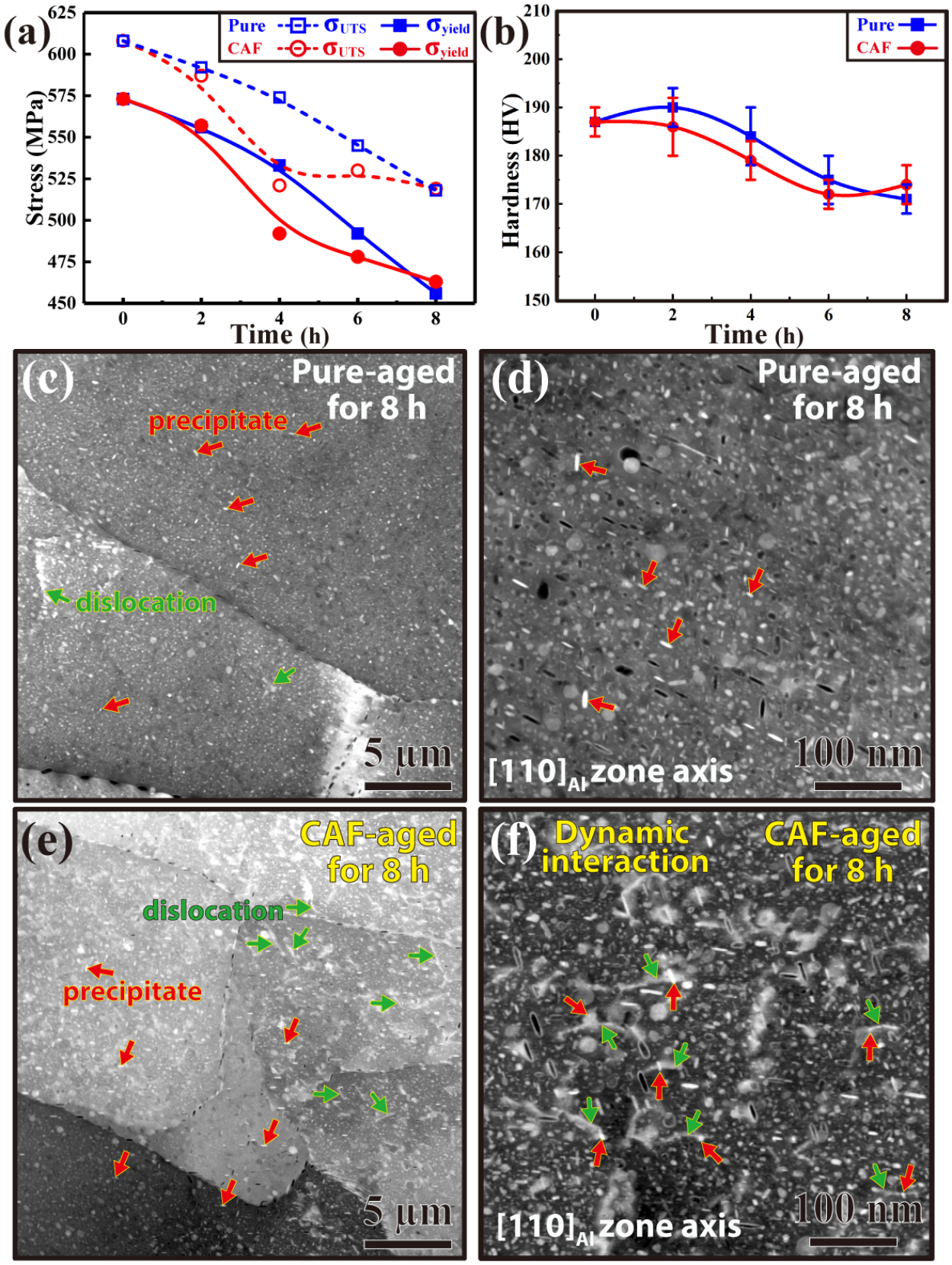

Fig. 1. (a, b) A comparison of the ultimate tensile strength (σ_{UTS}), yield strength (σ_{yield}) and hardness between the creep-age forming (CAF) samples and samples treated for the same ageing times (2, 4, 6 and 8 h) without stress (i.e., pure ageing). Low-magnification STEM images of the pure-aged samples treated for 8 h (c, d) and the CAF-aged samples treated for 8 h (e, f) showing the dislocations (indicated by green arrows) and the larger precipitates (indicated by red arrows) in the aluminium matrix. Especially, the dynamic interaction between dislocations and η precipitates in the aluminium matrix can be observed in (f).

3.2 Cs-corrected STEM observation of a perfect η-$MgZn_2$ crystal

Before further exploration of the evolution of atomic lattice defects within η precipitates induced by CAF, the 2-D Komura models and the atomic STEM image can be compared. As shown in Fig. 2a, each of these Komura units contains four structural layers [21], namely, the interwoven Mg/Zn/Mg/Zn atomic layers, located at z = 0, 3/8, 6/8, and 7/8, respectively, where Z is the level along [0001]η. The Zn layered structure (at z = 3/8) is characterized by the Kagomé net [21, 22] , and those of the other three layers, triangular nets [23], as shown in Fig. 2b. The rule of the stacking sequence among these six Komura units of Laves phases (Fig. 2c) [21, 33, 34, 38] is governed by the atomic displacements along 1/3 $[\bar{1}100]\eta$, resulting in A → B → C and A' → B' → C', and associated with the 6_3 screw axis along [0001]η, resulting in A → B', B → C', and C → A'. The resultant stackings for A combined with B', B combined with C', and C combined with A' are illustrated in Supplementary Fig. 3 in Supplementary Material. It should be noted that the AB', BC' and CA' stackings are indistinguishable in 2-D $RR^{-1}RR^{-1}$ atomic images under the atomic projection of the $[2\bar{1}\bar{1}0]$ zone axis. The atomic arrangement between A and B' is related to the symmetry operations of the $6_3/m$ axis along [0001]η, the 2/m axis along $[2\bar{1}\bar{1}0]\eta$, and the 2/c axis along $[10\bar{1}0]\eta$. In addition, mirror symmetry operations can be identified with respect to the $(1\bar{1}00)\eta$ plane between A|A', B|C', and B'|C [23]. In the present work, our results (as shown below) revealed that the possible configurations of η precipitates are presumed to be the main frames, zig-zag RR^{-1} structures, interwoven with $\cdots RR^{-1}RR\cdots$ and $\cdots RRR\cdots$ rhombic structures. The analysis procedure is illustrated as follows. A simulated atomic model with the Komura atomic arrays has been used to create the 3-D atomic

structures of η, followed by the 2-D atomic stacking constructions for comparison with HR HAADF STEM images. The atomic models with the Komura atomic arrays for the individual C14 (AB'), C36 (AB'A'C) and C15 (ABC) structures, projected onto the $(2\,\bar{1}\bar{1}\,0)\eta$ plane, can be respectively characterized as the $\cdots RR^{-1}RR^{-1}\cdots$, $\cdots RR^{-1}R^{-1}RRR^{-1}R^{-1}R\cdots$ and $\cdots RRRRRR\cdots$ rhombic stackings, as shown in Supplementary Fig. 1 in Supplementary Material. Thereby, the repeated $R^{-1}R^{-1}RR$ stackings of C36 structures and the RRR stackings of C15 can be distinguished from the zig-zag RR^{-1} stackings of C14 structures.

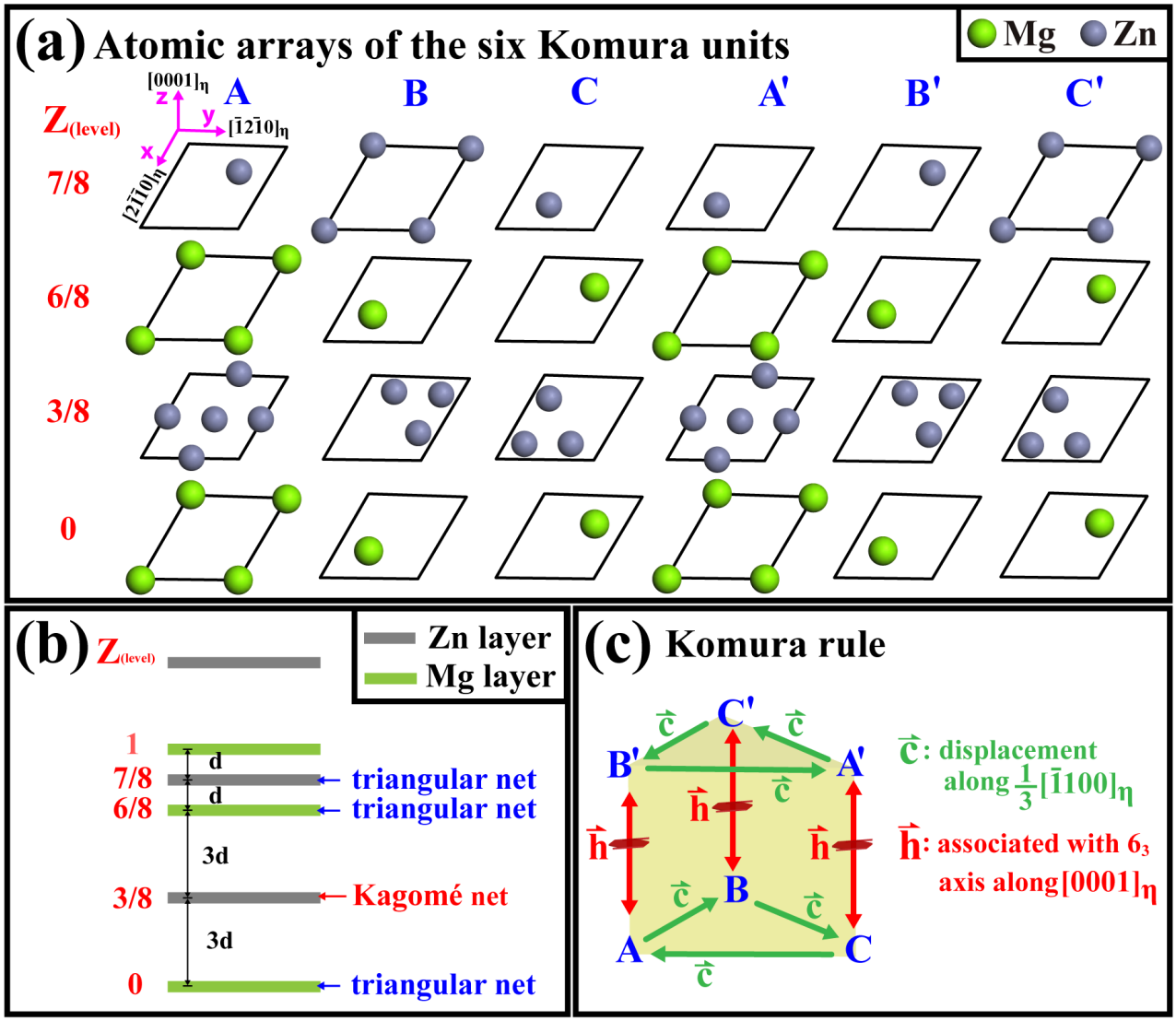

Fig. 2 Schematic diagram indicating (a) the six Komura units: A, B, and C and the A', B', and C'. (b) Each unit contains 4 layers with one Kagomé net and three triangular net configurations. (c) The Komura rule revealing the stacking sequence in between these six Komura units [21, 33, 34, 38].

Accordingly, Figs. 3a and b, reveal that the zig-zag rhombic arrangement (i.e., the $\cdots RR^{-1}RR^{-1}\cdots$ array) of a perfect η_2-$MgZn_2$ crystal can be fitted by C14 (AB') stacking [16, 25] under the observation of the $[2\bar{1}\bar{1}0]\eta$ zone axis. The AB' unit cells are constructed by VASP atomic model with the Komura atomic arrays (Fig. 1c) to stack A and B' units together along the $[0001]\eta$ axis, thereby creating the 3-D structure of η with the AB'AB' stacking. The 2-D projection of the AB'AB' stacking along the $[2\bar{1}\bar{1}0]\eta$ axis is then performed. As shown in Fig. 3c, the uniform $RR^{-1}RR^{-1}$ zig-zag stacking can be seen on the $(2\bar{1}\bar{1}0)\eta$ projection plane of the 3-D AB'AB' stacking sequence. Other 2-D projected rhombic stackings of the different types of η, which will be presented in the following section, are also reconstructed in the same way. In the projection model of the AB'AB' stacking (Fig 3c), the projected rhombic-unit (R) and the inversely projected rhombic-unit (R^{-1}) can be individually identified with four vertices of a rhombus, where the projection column of each vertex contains two Zn atoms and that of the midpoint at the rhombic edge, one Zn atom (as a unit cell of η_2 is considered). This result is significantly consistent with the Z-contrast atomic image in Fig. 3b. The corresponding unit cell of η_2 is marked by red squares outlined in blue in Figs. 3b and c. Moreover, the individual atoms of Zn and Mg in atomic columns with different levels along the direction $[2\bar{1}\bar{1}0]\eta$ of this HCP crystal (labelled by a fraction of a_1, where $a_1 = \frac{1}{3}[2\bar{1}\bar{1}0]$) are indicated by the differently-outlined circles in various shades of gray and green, as shown in Fig. 3c.

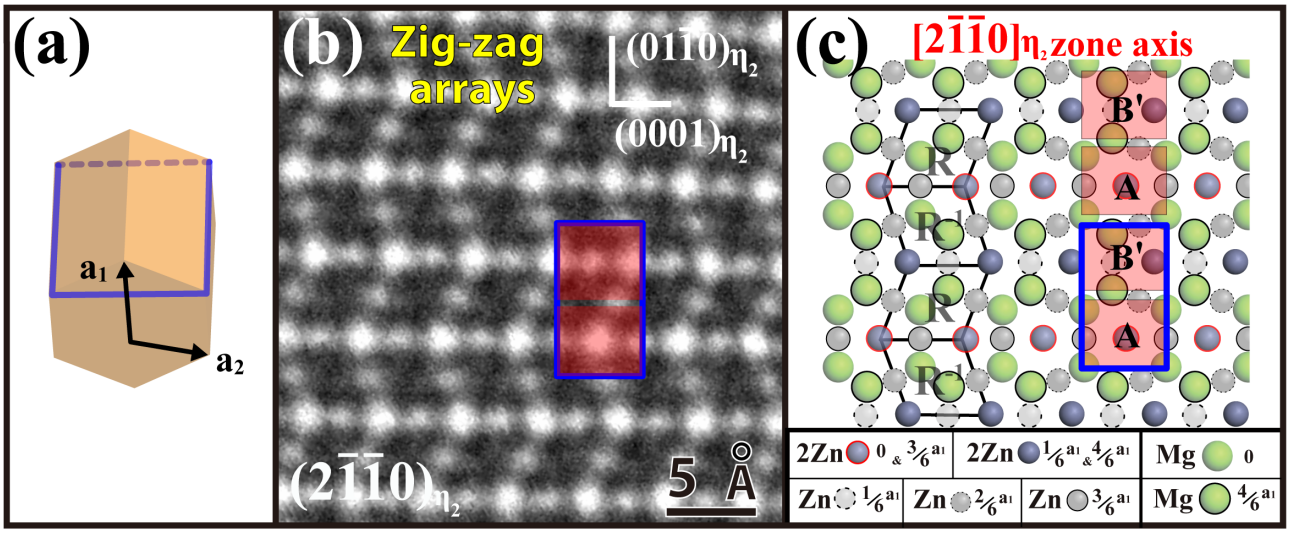

Fig. 3. HAADF-STEM images and atom projections of a perfect η-$MgZn_2$ crystal in creep-age forming (CAF) treated AA7050 aluminium alloy. (a) Profile of an HCP unit cell with the projection direction of [2$\bar{1}\bar{1}$0], where $a_1 = \frac{1}{3}[2\bar{1}\bar{1}0]$. (b) Under the $[2\bar{1}\bar{1}0]_{\eta_2}$ zone axis, the $(2\bar{1}\bar{1}0)_{\eta_2}$ image of η_2 showing the typical zig-zag configurations. (c) The simulated atomic arrays of the projection plane (2$\bar{1}\bar{1}$0) constructed by VASP atomic model with the Komura atomic arrays. The AB'AB' stacking sequence can thereby established. In the legend at the lower part of (c), the circles with varying shades of gray/green respectively point out the positions and numbers of Zn and Mg in their atomic columns in an AB' cell along the $\frac{1}{3}[2\bar{1}\bar{1}0]_{\eta_2}$ zone axis.)

3.3 CAF-induced atomic lattice defects of η

3.3.1 Atomic lattice defects of η under observation along the $[110]_{Al}$ zone axis

As shown in Fig. 4a, along the $[110]_{Al}$ zone axis, the zig-zag stackings pass almost all the way through the whole η precipitate, which presumably formed along the $(002)_{Al}$ plane. The corresponding FFT (fast Fourier transformation) diffractogram (Fig. 4b) with the simulated diffraction pattern (Fig. 4c) indicates that along the zone axis of $[110]_{Al}$ // $[2\bar{1}\bar{1}0]_{\eta}$, the $(0\bar{2}20)_{\eta}$ pole is exactly parallel to the $(002)_{Al}$ pole; the result is consistent with the orientation relationship of η_1 with respect to the aluminium matrix (Table 1). The elongated diffraction spots (Fig. 4b) are attributed to the shape factor of this given η_1. Additionally, the several rows of satellite spots are uniformly distributed along $[0\bar{2}20]_{\eta_1}$ // $[002]_{Al}$, indicated by yellow arrows in Fig. 4b. The nine uniform spacings among the transmitted beam and the satellite spots along the pole of $0\bar{2}20_{\eta_1}$ can be related to nine atomic layers of the $(0\bar{1}10)_{\eta_1}$ plane, as labelled by 1-9 in yellow in Figs. 4d and e, which were obtained from the

enlarged image on the left- and right- sides of Fig. 4a. For its atomic configuration, Figs. 4d and e, clearly reveal the layer-by-layer growth mechanism following the C14 (AB') stacking sequences [16]. However, the blurred Z-contrast atomic columns within the rhombic-unit (R) and the inversely rhombic-unit (R^{-1}) of η_1 can be identified and indicated by the purple arrows in Figs. 4d and e, as compared with the corresponding atomic columns in Fig. 3b. This would imply some characteristic atomic defects embedded along the atomic columns, leading to the change in the Z-contrast.

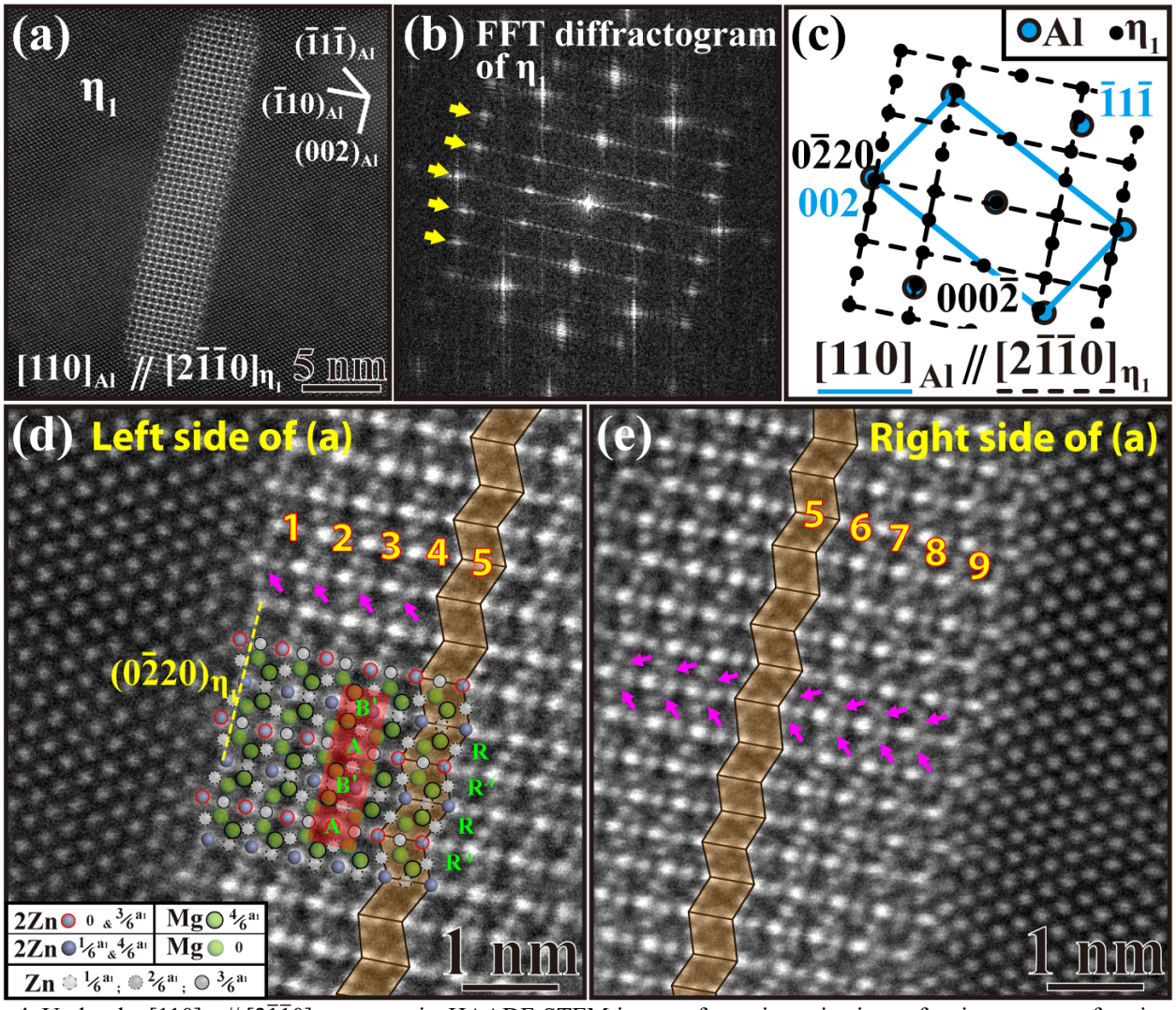

Fig. 4. Under the $[110]_{Al}$ // $[2\bar{1}\bar{1}0]\eta_1$ zone axis, HAADF-STEM image of atomic projections of η_1 in creep-age forming (CAF) treated AA7050 aluminium alloy. (a) The atomic projections of $(2\bar{1}\bar{1}0)\eta_1$ plane showing rod-like morphology with zig-zag rhombic stackings along the $(0001)\eta_1$ // $(\bar{2}20)_{Al}$ plane. (b, c) Corresponding FFT diffractograms and simulated diffraction patterns of (a) showing the orientation relationship of η_1, whereas (b) displaying several extra spots indicated by the yellow arrows. (d, e) Enlarged images of the left and right sides of (a) revealing the AB' stackings with respect to the RR^{-1} sequences, and also showing the characteristic atomic defects (indicated by purple arrows). In the legend at the lower part of (d), the circles in varying shades of gray/green respectively point out the positions and numbers of Zn and Mg atomic columns along the $\frac{1}{3}[2\bar{1}\bar{1}0]\eta_1$ axis.

Table 1 The 15 types of orientation relationships between η precipitates (η_1-η_{14} and η_4')[(a)] and aluminium matrix.

	Orientation relationship		Morphology	Ref.
η'[(b)]	$(0001)\eta' // (1\bar{1}\bar{1})_{Al}$	$[10\bar{1}0]\eta' // [110]_{Al}$	Hexagonal or rounded plate	[15, 17, 24, 25, 44-52]
η_1	$(10\bar{1}0)\eta_1 // (001)_{Al}$	$[2\bar{1}\bar{1}0]\eta_1 // [110]_{Al}$	Rod or plate	[15-17, 24, 44, 45, 50-56]
η_9	$(11\bar{2}0)\eta_9 // (001)_{Al}$	$[1\bar{1}00]\eta_9 // [110]_{Al}$	Hexagonal prism	[15-17, 24, 45, 57]
η_2	$(0001)\eta_2 // (1\bar{1}\bar{1})_{Al}$	$[10\bar{1}0]\eta_2 // [110]_{Al}$	Hexagonal or rounded plate	[15-17, 24, 25, 44-47, 50, 51, 53]
η_3	$(0001)\eta_3 // (1\bar{1}\bar{1})_{Al}$	$[2\bar{1}\bar{1}0]\eta_3 // [110]_{Al}$	Hexagonal or triangular plate	[15-17, 24, 44, 45, 50]
η_{10}	$(0001)\eta_{10} // (1\bar{1}\bar{1})_{Al}$	$[2\bar{1}\bar{1}0]\eta_{10} // [1\bar{3}4]_{Al}$	Not indicated[(a)]	[15-17, 45, 50]
η_{11}	$(0001)\eta_{11} // (110)_{Al}$	$[10\bar{1}0]\eta_{11} // [1\bar{1}\bar{1}]_{Al}$	Rod	[15-17, 50]
η_4	$(0001)\eta_4 // (110)_{Al}$	$[2\bar{1}\bar{1}0]\eta_4 // [1\bar{1}\bar{1}]_{Al}$	Rod	[15-17, 24, 44, 45, 47, 50-52]
η_4'	$(0001)\eta_4' // (110)_{Al}$	$[1\bar{1}00]\eta_4' // [001]_{Al}$	Hexagonal plate or prism	[16]
η_5	$(\bar{1}2\bar{1}0)\eta_5 // (1\bar{1}\bar{1})_{Al}$	$[30\bar{3}2]\eta_5 // [110]_{Al}$	Rod	[15-17, 24, 44, 47, 50]
η_6	$(\bar{1}2\bar{1}0)\eta_6 // (1\bar{1}\bar{1})_{Al}$	$[20\bar{2}1]\eta_6 // [1\bar{1}2]_{Al}$	Rod	[15-17, 24, 44, 47, 50]
η_7	$(\bar{1}2\bar{1}0)\eta_7 // (1\bar{1}\bar{1})_{Al}$	$[10\bar{1}4]\eta_7 // [110]_{Al}$	Rod	[15-17, 24, 44, 47, 50]
η_8	$(\bar{1}2\bar{1}0)\eta_8 // (1\bar{1}2)_{Al}$	$[0001]\eta_8 // [31\bar{1}]_{Al}$	Rod	[15, 17, 24, 44, 50]
η_{12}	$(0001)\eta_{12} // (1\bar{1}\bar{3})_{Al}$	$[2\bar{1}\bar{1}0]\eta_{12} // [110]_{Al}$	Plate	[16]
η_{13}	$(0001)\eta_{13} // (042)_{Al}$	$[2\bar{1}\bar{1}0]\eta_{13} // [100]_{Al}$	Rod	[19] & Present work
η_{14}[(c)]	$(0001)\eta_{14} // (51\bar{3})_{Al}$	$[2\bar{1}\bar{1}0]\eta_{14} // [112]_{Al}$	Plate	Present work

(a) The notations from η_1-$_{11}$ were used by Degischer et al. [17]. Similar data were tabulated by Bendo et al. [19, 24] and Chung et al. [15, 16]. The morphology of η_{10} has yet to be identified by TEM and HAADF STEM.
(b) The orientation relationship and morphology of η' are listed for reference.
(c) A novel η_{14}-type precipitate was first analyzed in the present work.

Under the observation along the zone axis of $[110]_{Al} // [2\bar{1}\bar{1}0]\eta$, a given particle exhibits nearly zig-zag rhombic stackings interwoven with irregular sub-unit defect chains (indicated by the yellow arrows in Fig. 5a) can be identified. Additionally, the Penrose tiling features are accompanied by the differently-oriented elongated hexagonal defects and rhombic units (indicated by the red arrows in Fig. 5a). These elongated hexagonal defects are denoted as hexagonal Type I defects [16]. Furthermore, this precipitate possesses the same orientation relationship of η_1 with respect to the

aluminium matrix (as analysed in Figs. 5b and c). However, it is worth noting that this given η_1 displays the nearly spherical-like morphology, which is obviously different from the plate-like morphology of the typical η_1 having a higher aspect ratio (Fig. 4). Fig. 5d (the enlarged image of Fig. 5a) and Fig. 5e (the simulated atomic arrays of Fig. 5d) illustrate the connection of zig-zag rhombic stackings to the sub-unit defect chains (marked in pink and red). Obviously, the regular zig-zag rhombic stackings are interrupted by faulted layers (as indicated by yellow arrows in Fig. 5d). It is presumed that several embryos of η_1 (labelled #1, #2, and #3 in Fig. 5d) initially nucleated on the $(0002)\eta_1$ // $(\bar{1}10)_{Al}$ plane and then laterally grew along the $[0002]\eta_1$ // $[\bar{1}10]_{Al}$ direction. Here, it is assumed that the zig-zag configuration of η_1 on the $(2\bar{1}\bar{1}0)\eta$ projection plane is based on the C14 (AB') stackings. As shown in Fig. 5e, atomic arrangements of embryos #1, #2, and #3 regions are reconstructed by the model of Komura atomic arrays. In the junction areas, the elongated hexagonal defects can conform to the development of rhombic stackings of embryos, accompanied by the change in the stacking sequence; i.e., the uncompleted C36 stacking ($\underline{AB'A'^{\downarrow}_{\uparrow}}$) is incorporated into the AB'AB' stacking ($AB'\underline{AB'A'^{\downarrow}_{\uparrow}}AB'$), as illustrated in Fig. 5e. Additionally, the main axis of the elongated hexagon unit, which is located between the #1 and #2 embryos (as shown in Fig. 5e), possesses a small deviation angle of ~9° with respect to the $(0\bar{2}20)\eta_1$ broad facet. However, for another elongated-hexagon defect, which is located between the #2 and #3 embryos (as shown in Fig. 5e), its main axis has a large deviation angle of ~54° with respect to the $(0\bar{2}20)\eta_1$ broad facet.

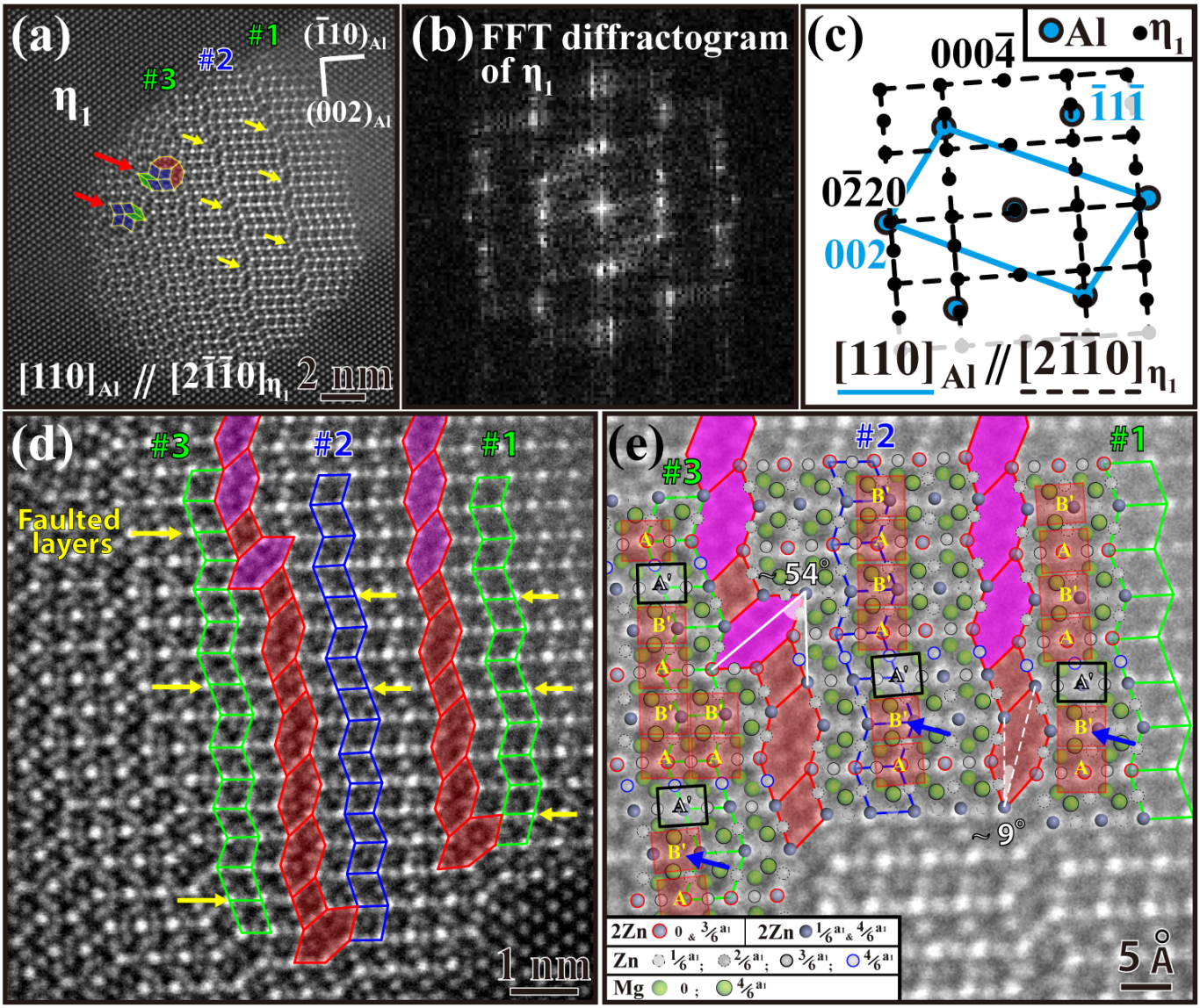

Fig. 5. Under the $[110]_{Al}$ // $[2\bar{1}\bar{1}0]\eta_1$ zone axis, HAADF-STEM image of atomic projections of η_1 in creep-age forming (CAF) treated AA7050 aluminium alloy. (a) The atomic projections of $(2\bar{1}\bar{1}0)\eta_1$ plane showing nearly zig-zag rhombic stackings interwoven with irregular sub-unit chains (marked by the yellow arrows). In the left side region of (a), two Penrose tiling features (marked by the red arrows) accompanied by elongated hexagonal defects can be identified. (b, c) The corresponding FFT diffractograms and simulated diffraction patterns of (a) showing the orientation relationship of η_1 with respect to the Al matrix. (d) The enlarged image of (a) illustrating the connection of the zig-zag rhombic stackings of three η_1 embryos, labelled #1, #2, and #3 to the irregular sub-unit defect chains (marked in pink and red) and the faulted layers (indicated by yellow arrows). (e) Atomic arrangements of #1, #2, and #3 regions constructed by the model of Komura atomic arrays.

In Fig. 6, under the zone axis of $[110]_{Al}$ // $[2\bar{1}\bar{1}0]\eta$, the $(2\bar{1}\bar{1}0)$ atomic projection of η reveals zig-zag rhombic stacking structures interwoven with the irregular sub-unit defects (indicated by the red and green arrows in Fig 6a). It can also be observed that the similar Penrose tiling features, especially the five-fold configuration, are accompanied by differently-oriented elongated hexagonal defects (indicated by the blue arrows in Fig. 6a). Apparently, the regular zig-zag stackings are interrupted by faulted layers, as indicated by yellow lines in Fig. 6a. Consistent with the previous result [16], the FFT diffractograms (Fig. 6b) and the simulated diffraction patterns (Fig. 6c) indicate that this precipitate would possess the orientation relationship of η_{12} with respect to the Al matrix, i.e., $[110]_{Al}$ // $[2\bar{1}\bar{1}0]\eta_{12}$ and $(1\bar{1}\bar{3})_{Al}$ // $(0001)\eta_{12}$ (Table 1). Here, it is assumed that the zig-zag configuration of η_{12} on the $(2\bar{1}\bar{1}0)\eta$ projection plane is based on the C14 (AB') stackings. Fig. 6d, the enlarged image of the marked red and green elongated-hexagons in Fig. 6a, shows the faulted layer nearby those elongated-hexagon defects. This faulted layer with A' type unit (indicated by the yellow line in Figs. 6a and d), interwoven with the repeated zig-zag rhombic array, is tentatively ascribed to the uncompleted C36 stacking (i.e., $\underline{AB'A'}^{\downarrow}_{\downarrow}$), followed by the C14 (AB') stacking, as shown in Fig. 6d. Notably, two types of elongated hexagonal defects in Fig. 6a denoted as Type I (marked green) and Type II (marked red) defects are enlarged and characterized in Figs. 6d and e. The Type I defect has a smaller main axis (~1.19 nm) accommodating 4 Mg atoms along its axis direction, and the Type II defect, a longer main axis (~1.69 nm), accommodating 6 Mg atoms along its axis direction. This hexagonal Type II defect is found within η_{12} for the first time in the present work. As shown in Fig. 6e, the Type I elongated hexagonal defect possesses nearly the same edges (occupied by Zn atoms)

with inner angles of 144° and 72°. Alternatively, Type II elongated hexagonal defect can be outlined by two longer and four smaller edges (occupied by Zn atoms) with the same inner angles with respect to those of the Type I elongated hexagonal defect. The projection column of each vertex contains two Zn atoms as a unit cell of C14 (AB') stackings is considered. The possible atomic numbers of the Type I elongated hexagonal array are estimated to be 6 Mg atoms and 7–8 Zn atoms, and those of the Type II elongated hexagonal array, 10 Mg atoms and 8–9 Zn atoms, as shown in Fig. 6e, respectively.

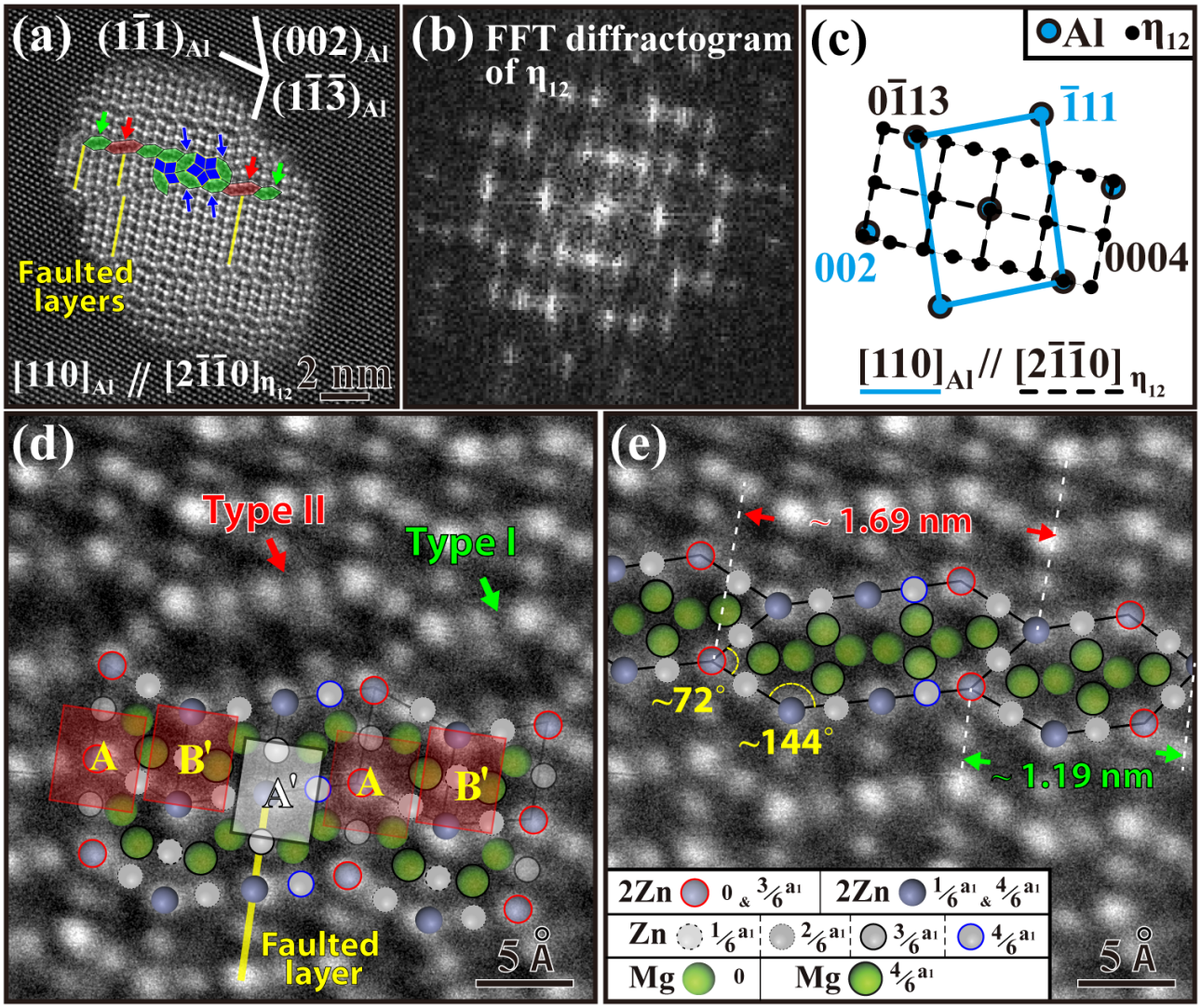

Fig 6. Under the $[110]_{Al}$ // $[2\bar{1}\bar{1}0]\eta_{12}$ zone axis, HAADF-STEM image of atomic projection of η_{12} in creep-age forming (CAF) treated AA7050 aluminium alloy. (a) The atomic projection of $(2\bar{1}\bar{1}0)\eta_1$ plane of η_{12} showing rhombic zig-zag stacking structures interwoven with the irregular sub-unit defects (indicated by the red and green arrows) and the faulted layers (indicated by yellow lines). (b, c) The corresponding FFT diffractogram and simulated diffraction pattern of (a) showing the orientation relationship of η_{12} with respect to the aluminium matrix. The image of Type I (marked green) and II (marked red) the elongated hexagonal defects in (a) being enlarged, as presented in (d, e). (d) showing atomic arrangements of the adjacent area, and (e) showing the atomic arrangements of Type I and Type II.

3.3.2 Atomic lattice defects of η under observation along the $[100]_{Al}$ zone axis

A previous work on the investigation of η_{13} precipitates subjected to artificial ageing treatment [19] reported that along the zone axis of $[100]_{Al}$ // $[2\bar{1}\bar{1}0]\eta_{13}$, the $(2\bar{1}\bar{1}0)\eta$ atomic projection of η_{13}, displays the habit plane $(021)_{Al}$ // $(0001)\eta_{13}$ and the entire zig-zag stacking without any elongated hexagonal defects. However, for the investigation of the dynamic precipitation of CAF in the present work, it is herein reported for the first time that the η_{13} precipitate possesses irregular sub-unit defect chains, as indicated by the green arrow in Fig. 7a. The regular zig-zag stacking is interrupted by the faulted layers, as indicated by yellow arrows. From the corresponding FFT diffractograms (Fig. 7b) and the simulated diffraction patterns (Fig. 7c), the orientation relationship of the η precipitate is the same as that of η_{13} i.e., $(042)_{Al}$ // $(0004)\eta_{13}$ and $[100]_{Al}$ // $[2\bar{1}\bar{1}0]\eta_{13}$, and the result is listed in Table 1. Here, it is assumed that the zig-zag configuration of η_{13} on the $(2\bar{1}\bar{1}0)\eta$ projection plane is based on the C14 (AB') stacking. As shown in Fig. 7d, the enlarged image of Fig. 7a clearly indicates the differently-oriented elongated hexagonal defects (Type I) and rhombic units along the irregular sub-unit defect chain. Adjacent to this chain area, the atomic arrangements by using the model of Komura atomic arrays were constructed and the possible unit stackings C14-C15-A'-C14 are depicted in Fig. 7e.

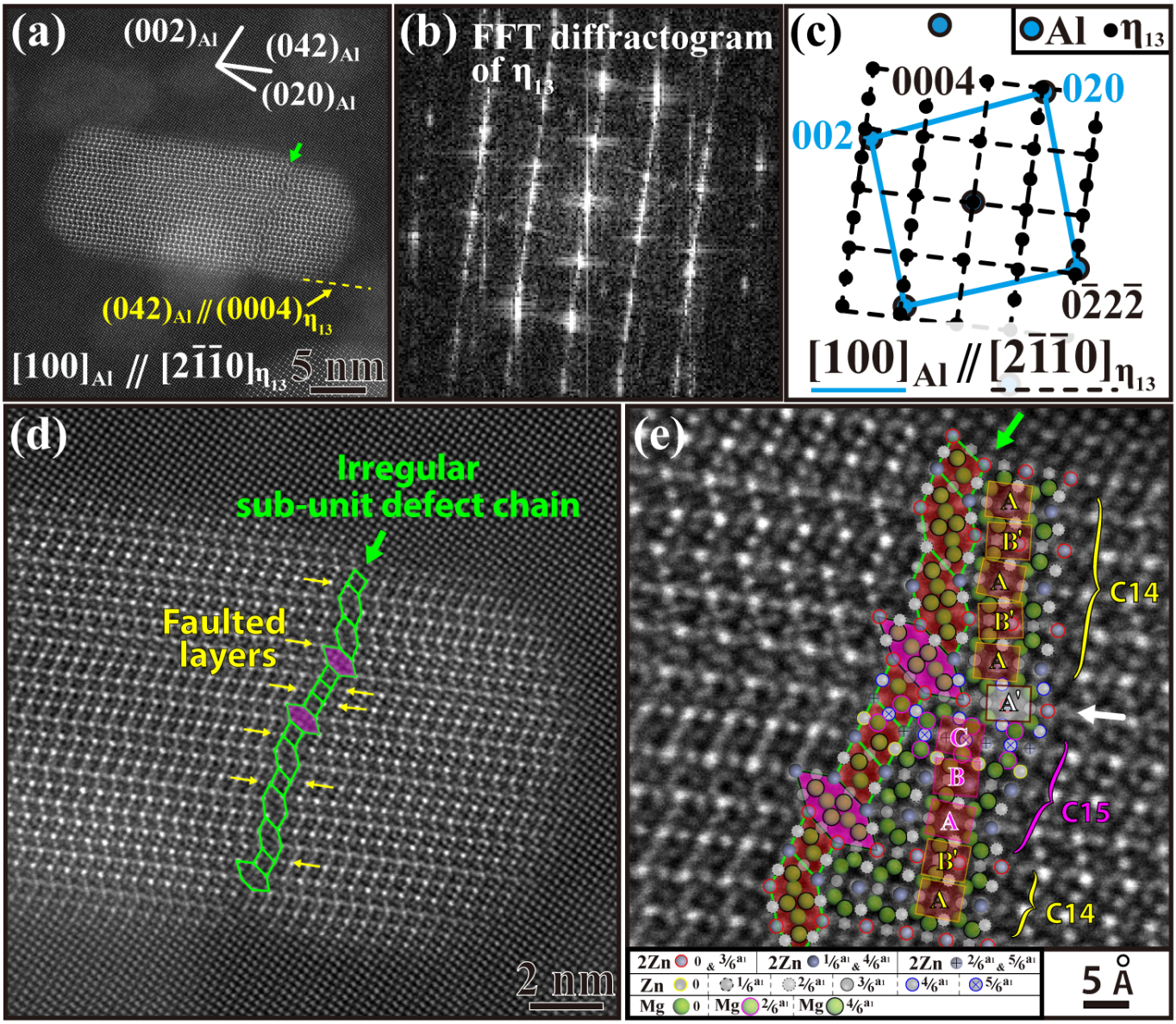

Fig. 7. Under the $[100]_{Al}$ // $[2\bar{1}\bar{1}0]\eta_{13}$ zone axis, HAADF-STEM image of and atomic projections of η_{13} in creep-age forming (CAF) treated AA7050 aluminium alloy. (a) The $(2\bar{1}\bar{1}0)$ atomic projection showing the zig-zag rhombic stackings with the irregular sub-unit defect chain (as indicated by the green arrow). (b, c) FFT diffractograms and simulated diffraction patterns of (a) showing the orientation relationship of η_{13} with respect to the aluminium matrix. (d) Enlarged images of (a) showing the irregular sub-unit defect chain accompanied by the faulted layers (indicated by yellow arrows), and (e) the atomic arrangements of the area adjacent to the defect chain being constructed by the model of Komura atomic arrays and the possible unit stacking C14-C15-A'-C14 being displayed.

3.3.3 Atomic lattice defects of η under observation along the $[112]_{Al}$ zone axis

Fig. 8a shows another case to illustrate the hexagonal Type I defects in η_2, where the zone axis of $[112]_{Al}$ // $[2\bar{1}\bar{1}0]\eta_2$ brings about the edge-on configuration of the $(11\bar{1})_{Al}$ // $(0001)\eta_2$ habit plane. The corresponding FFT diffractogram (Fig. 8b) and the simulated diffraction pattern (Fig. 8c) show the orientation relationship of η_2 with respect to the aluminium matrix (as listed in Table 1). Furthermore, in Fig. 8a, it is revealed that along the transformation front of η_2 on the $(11\bar{1})_{Al}$ // $(0001)\eta_2$ plane, two ledges (as indicated by the solid and dotted green arrows in Fig. 8a, respectively) are connected with the irregular sub-unit defect chains, which are composed of the hexagonal Type I defects and the rhombic units, similarly to η_1 (as shown in Fig. 5). Fig. 8d (the enlarged image of Fig. 8a) displays the detailed atomic columns of the rhombic stackings nearby the irregular sub-unit defect chain with the accompanying faulted layers (indicated by yellow arrows). Here, it is assumed that the zig-zag configuration of η_2 on the $(2\bar{1}\bar{1}0)\eta$ projection plane is based on the C14 (AB') stackings. The atomic arrangements of the area adjacent to the irregular sub-unit defect chain were reconstructed and the possible arrays are depicted in Figs. 8d and e. The more detailed different atomic distributions with the levels along the observation direction are portrayed in Supplementary Fig. 4 in Supplementary Material. Furthermore, under the zone axis of $[112]_{Al}$ // $[2\bar{1}\bar{1}0]\eta_2$, where $(11\bar{1})_{Al}$ matrix plane is in an edge-on configuration, it is hard to observe the diffusion paths of Zn/Cu atoms along $(11\bar{1})_{Al}$ matrix plane, which is parallel to the transformation front $(0001)\eta_2$, as shown in Figs 8a and d.

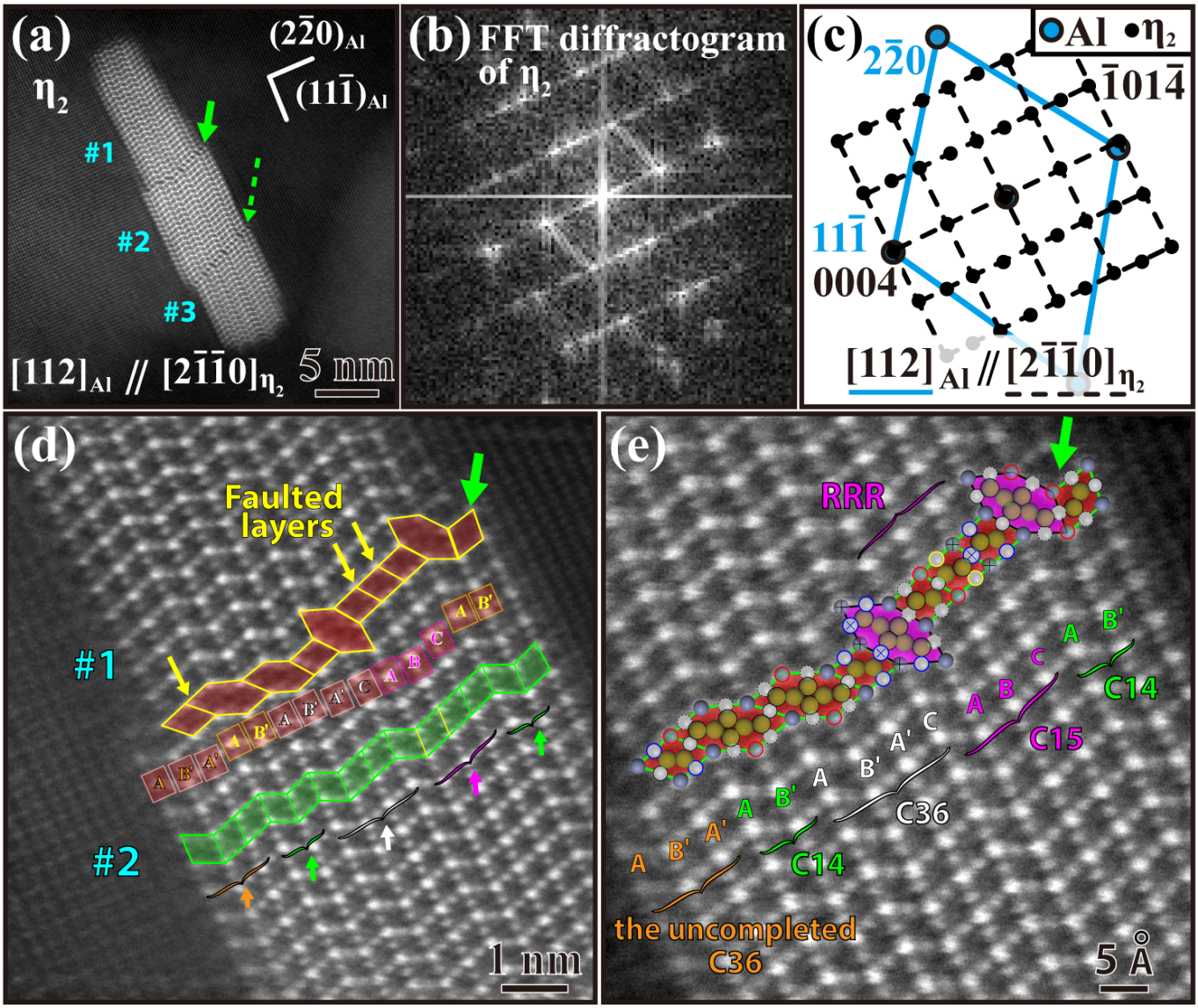

Fig. 8. Along the $[112]_{Al}$ // $[2\bar{1}\bar{1}0]\eta_2$ zone axis, HAADF-STEM images and atom projections of η_2 in creep-age forming (CAF) treated AA7050 aluminium alloy. (a) The $(2\bar{1}\bar{1}0)$ atomic projection showing the zig-zag rhombic stackings with the irregular sub-unit defect chains (as indicated by solid and dotted arrows in green). (b) and (c) The corresponding FFT diffractograms and simulated diffraction patterns of (a), showing the orientation relationship of η_2 with respect to the aluminium matrix. (d) and (e) The enlarged images of (a) and (d) showing the detailed atomic columns of the rhombic stackings nearby the irregular sub-unit defect chain with the accompanying faulted layers (indicated by yellow arrows). The atom arrangements of the adjacent area being constructed by the model of Komura array model and the possible unit stacking being displayed: the uncompleted C36 ($\underline{AB'A'}^{\downarrow}_{\uparrow}$), C14 (AB'), C36 (AB'A'C) with C15 (ABC).

A striking example of HR-STEM image in Fig. 9 illustrates the zig-zag rhombic stacking structure accompanied by two entirely-passed stacking fault layers and also reveals the diffusion paths of Zn/Cu atoms adjacent to the transformation front. Along the zone axis of $[112]_{Al}$ // $[2\bar{1}\bar{1}0]\eta$, the $(2\bar{1}\bar{1}0)\eta$ atomic projection shows zig-zag stacking as shown in Fig. 9a. The corresponding FFT diffractograms and the simulated diffraction patterns are shown in Fig. 9b. Fig. 9c, the enlarged image of the FFT diffractograms in Fig. 9b reveals that the pole of $51\bar{3}_{Al}$ of the aluminium matrix (blue arrow) is nearly parallel to the 0004η pole of the precipitate (red arrow in the revised Fig. 9c). Thus, the orientation relationship of this precipitate with respect to the aluminium matrix is determined to be $[112]_{Al}$ // $[2\bar{1}\bar{1}0]\eta$ and $(51\bar{3})_{Al}$ // $(0002)\eta$, and it can be regarded as a new type of η. Thus, this new type of precipitate is named η_{14}, and its orientation relationship with the aluminium matrix is listed in Table 1. The image of Fig. 9a is enlarged and presented in Fig. 9d; it shows that the zig-zag stacking is interrupted by two faulted layers (as highlighted in green in Figs. 9a and d). Here, the regular zig-zag configuration of η_{14} on the $(2\bar{1}\bar{1}0)\eta$ projection plane is also considered on the basis of the C14 (AB') stackings. The atomic arrangements in between the stacking faults and their adjacent areas were reconstructed by the model of Komura atomic arrays, as illustrated in Fig. 9d. These faulted layers nearly along the $(0002)\eta_{14}$ // $(51\bar{3})_{Al}$ plane are not accompanied by the elongated hexagonal defects. On the other hand, based on the HAADF-STEM imaging, the Z-contrast of the individual atomic column is roughly proportional to the square of Z (atomic numbers of atoms) and also related to the number of atoms in each atomic column [58]. Owing to the chemical composition of the AA7050 aluminium alloy (Al-6.25Zn-2.14Mg-2.23Cu (wt.%)) investigated in the present work, the solute

atoms in the aluminium matrix include Zn, Mg and Cu atoms. The Z-contrast of Al^{13}, Zn^{30}, Mg^{12} and Cu^{29} exhibits a ratio of approximately 169: 900: 144: 841. Under the zone axis of $[112]_{Al}$, Fig. 9e reveals that in the matrix away from the η_{14} precipitate (Fig. 9e), the lower Z-contrast of the atomic columns can be suggested to be associated with Al or Mg atoms. On the other hand, in the matrix adjacent to the transformation front of the η_{14} precipitate, the higher Z-contrast of the atomic columns is probably due to Zn or Cu atoms. Therefore, the diffusion paths of Zn/Cu atoms on the $(11\bar{1})_{Al}$ planes close to the transformation front can clearly be observed. The intensity line profiles of the HR-STEM image, revealing Z-contrast gradients in aluminium matrix approaching the transformation fronts of η_{14} precipitates, are presented in Supplementary Fig. 5 in Supplementary Material.

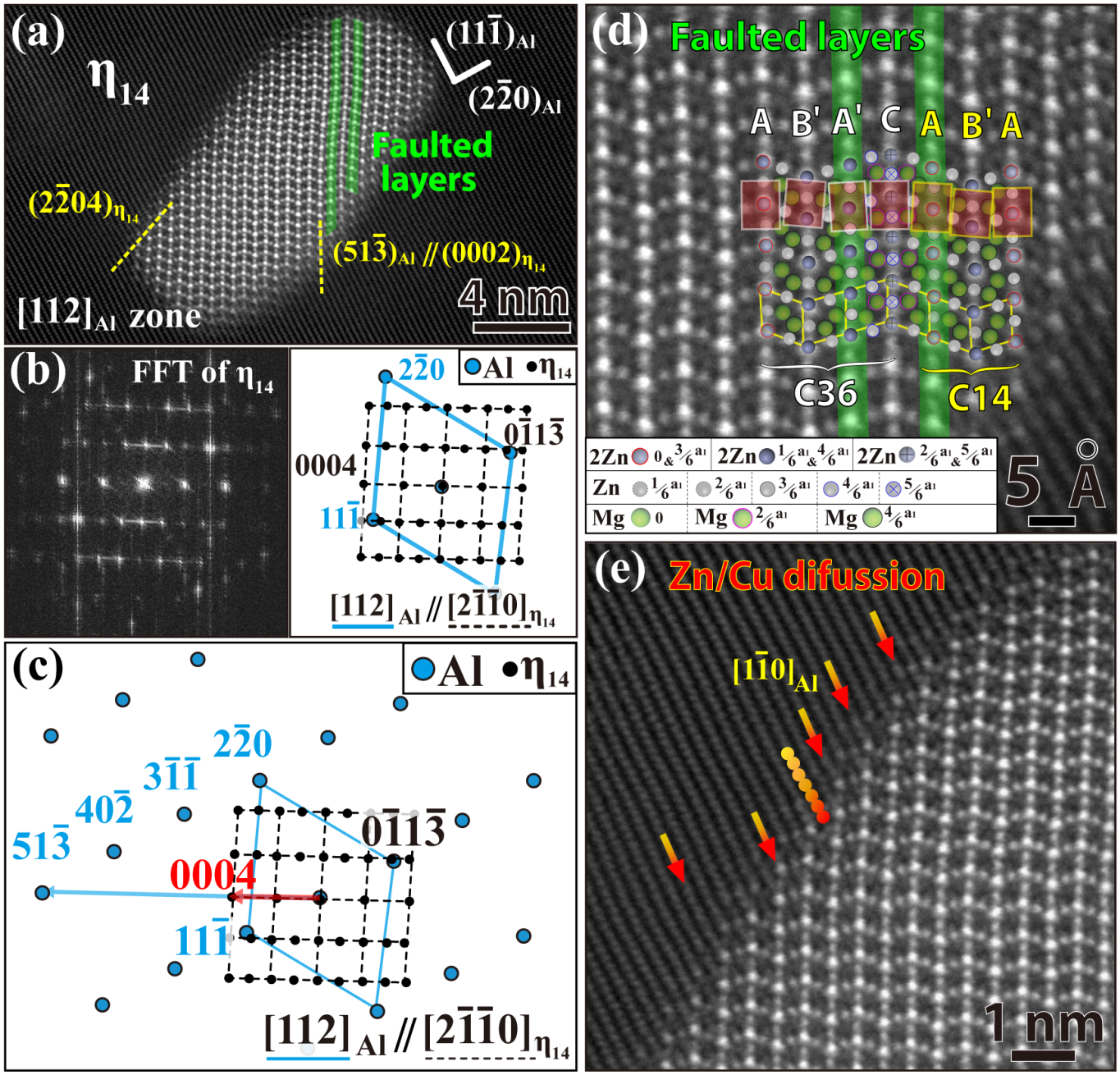

Fig. 9. Under the $[112]_{Al}$ // $[2\bar{1}\bar{1}0]\eta_{14}$ zone axis, HAADF-STEM image of atomic projections of η_{14} in creep-age forming (CAF) treated (AA7050 aluminium alloy. (a) η_{14} with the zig-zag rhombic stacking structures accompanied by two entirely-passed faulted layers, as indicated by green lines. (b) The corresponding FFT diffractograms and simulated diffraction patterns of (a). (c) The enlarged image of FFT diffractograms in (b) showing the orientation relationship of η_{14} with respect to the aluminium matrix. (d) The enlarged image of (a) illustrating the C14 stacking structure interwoven with the C36 (AB'A'C) structure. The atomic arrangements were constructed by using the model of Komura atomic arrays. (e) The enlarged image of (a) illustrating the Zn/Cu diffusion paths along the $(11\bar{1})_{Al}$ plane in the matrix adjacent to the transformation front of η_{14}, as indicated by arrows with the gradient from yellow to red (low to high intensity). A row of colored dots displays the higher atomic number atoms enriched at the transformation front.

4. Discussion

Some previous works [9, 11, 59] on the precipitation in Al-Zn-Mg-Cu aluminium alloys subjected to creep-age forming (CAF) have been reported. The mechanical properties of these CAF-treated alloys are correlated with the dislocations and precipitate size distribution at the micro-meter, but no research has focused on the changes in the atomic stackings of precipitates at the atomic scale. In the present work, the evolution of precipitates, investigated by mechanical tests, and the atomic configurations of different-typed η, determined by HAADF-STEM and structural modelling, provide new insights into the arrays of atomic lattice defects within η precipitates due to the dynamic precipitation which occurs during CAF.

4.1 Relationship among mechanical strengthening, dislocations, and the structural evolution of precipitates

It has been reported that the mechanical properties of Al-Zn-Mg-Cu alloys are presumably dominated by the contribution of η' and η precipitates [18, 60]. According to the SAXS model analysis (as shown in Supplementary Fig. 3 and Supplementary Table 1 in Supplementary Material), in the pure-aged condition, the diameters and thicknesses of η' and η precipitates, which are considered with the morphology of discs, roughly grow with ageing time, especially the thickness. In the CAF-aged condition, the sizes of η' and η are approximately the same as those of the pure-aged condition. However, the volume fraction by which η precipitates increase with increases in ageing time (due to η' → η) in the CAF-aged condition is significantly larger than that in the pure-aged condition (as shown in Supplementary Table 1 in Supplementary Material). It is suggested that the transformation

of η' → η is promoted by the creep-aged forming stress and leads to the lower mechanical strengths of 2, 4 and 6 h CAF-aged samples than those of 2, 4 and 6 h pure-aged samples (Figs. 2a and b). However, for 8 h CAF-aged and 8 h pure-aged samples, the mechanical strengths (Figs. 2a and b) are nearly the same. It is appropriate to conclude that 8 h CAF-aging brings about a significant amount of newly-formed dislocations, which profoundly promote the interaction between themselves and precipitates (Figs. 2e and f). On the other hand, the dynamic interaction between precipitates and dislocations presumably leads to the formation of atomic lattice defects within the η precipitates (as shown in Figs. 5-9).

4.2 Relationship between CAF-induced lattice defects and atomic stackings

In previous works [61-63], HRTEM indicated that β_2'-$MgZn_2$ precipitates of Mg-Zn(-Y) magnesium alloys exhibited zig-zag configurations under observation along the $[2\bar{1}\bar{1}0]$ zone axis of β_2'. These configurations are similar to those of η-$MgZn_2$ exhibiting zig-zag (RR^{-1}) arrays in Al-Zn-Mg-Cu aluminium alloys [16, 19, 25, 26]. However, in those HRTEM images [61-63], the numbers of atoms in each column of β_2' could not be evaluated from their corresponding phase contrast. The HAADF-STEM images, referring to Z-contrast, and the simulated 3-D crystal structures, referring to VASP calculation, are indispensable techniques for identifying the positions and number of atoms in each column in HR HAADF-STEM images. Along the zone axis of $[2\bar{1}\bar{1}0]\eta_2$, the $(2\bar{1}\bar{1}0)\eta_2$ image of perfect η-$MgZn_2$ exhibiting zig-zag (RR^{-1}) rhombic stackings can be assembled by the C14 (AB') stacking of the Laves phase (as shown in Fig. 3).

In the present work, all the observed samples were treated by CAF, and the forming stress presumably played an important role in the dynamic interaction between dislocations and precipitates. As shown in Fig. 4a, under observation along the $[2\bar{1}\bar{1}0]\eta_1$ // $[110]_{Al}$ zone axis, the zig-zag rhombic stacking passes almost all the way through the whole η_1 precipitate, which can also be expressed as the C14 (AB') stacking according to Komura's model [21]. However, in contrast to the perfect zig-zag (RR^{-1}) arrays (as shown in Fig. 3b), the enlarged image of η_1 (as shown in Figs. 4d and e) reveals the atomic columns, which are located within the rhombic-unit (R) and the inversely rhombic-unit (R^{-1}), with the diffused Z-contrast, as indicated by purple arrows. It is presumed that the periodic arrays of defects, i.e., the ordering defects [64], have been introduced. Consequently, several rows of satellite spots uniformly distributed along $[0\bar{2}20]\eta_1$ // $[002]_{Al}$ occurs, as shown in Fig. 4b. The nine uniform spacings between the satellite spots along the pole of $(0\bar{2}20)\eta_1$ can be related to the same number of atomic layers of the $(0\bar{1}10)\eta_1$ plane of the precipitate observed. In previous works [24, 28, 65], similar satellite spots were also found in the FFT diffractograms of η in Al-Zn-Mg(-Cu) aluminium alloys [24, 28, 65] and β_1' in Mg-Zn magnesium alloys [28]. However, the ordering defects were not reported in those works [24, 28, 65].

Furthermore, under observation along the zone axes of $[2\bar{1}\bar{1}0]\eta_1$ // $[110]_{Al}$, a special feature of the η_1 precipitate can be seen in Fig. 5. This complex atomic configuration of η_1 consist of the typical zig-zag rhombic stackings interwoven with the lattice defect chains, which are composed of the differently-oriented elongated hexagonal Type I defects alternating with rhombic units. These sub-unit chains substantially separate the η_1 precipitate into different regions (labelled #1, #2, and #3 in

Fig. 5d), where the regular zig-zag rhombic stackings are interrupted by faulted layers (indicated by yellow arrows). The change in the C14 stacking (AB'AB'…) is illustrated in Fig. 5e to explore the accommodation between the lattice defect chain and the zig-zag region. For example, in region #3, the B' unit of the AB' stacking (marked by the blue arrow in Fig. 5e) is inferred to be followed only by A or A' units according to Komura's rule (Fig. 1c). The projected unit (framed by black in Fig. 5e) has been found to exhibit the same $(2\bar{1}\bar{1}0)\eta$ projected configuration of the A' unit. Thus, this follow-up unit (framed by black in Fig. 5e) is presumed to be A'. Furthermore, the next follow-up $(2\bar{1}\bar{1}0)\eta$ projected unit, which directly connects after the A' unit (framed by black in Fig. 5e), is identified as an A unit, which is followed by a B' unit. Accordingly, the uncompleted C36 stacking forms with the AB'A' stacking can be established. The junction (as indicated by double arrows in AB'A'$\downarrow\uparrow$AB') between the uncompleted C36 (AB'A') stacking and the regular C14 (AB') stacking is presumably associated with the formation of the elongated hexagonal lattice defect, leading to the accommodation of lattice strain during CAF.

On the other hand, in the present work, the atomic configuration of η_{12} in the $(2\bar{1}\bar{1}0)\eta_{12}$ image observed along the $[110]_{Al}$ zone axis (Fig. 6) reveals the first reported hexagonal Type II defects in the sub-unit defect chain. This hexagonal Type II defect with a higher aspect ratio is similar to the sub-unit structure of the T phase ($Al_{20}Cu_2Mn_3$) of the Al-Cu-Mg-Ag aluminium alloys [66, 67]. It is also found that the zig-zag rhombic stacking of η_{12} was interrupted by several faulted layers (indicated by yellow lines in Fig. 6a), which are connected with the elongated hexagonal Type II lattice defects (marked red in Fig. 6a). The atomic arrays adjacent to Type I and Type II elongated hexagonal defects

have been investigated and illustrated in Fig. 6d. Followed by the AB' stacking, the $(2\bar{1}\bar{1}0)\eta$ projection unit (framed by black in Fig. 6d) exhibits the same $(2\bar{1}\bar{1}0)\eta$ projected configuration of an A' unit. In the follow-up stackings, the A' unit is not followed by the C or C' units (according to Komura's rule) but directly connects with an A unit, leading to the $AB'A'^{\downarrow}_{\uparrow}AB'$ stacking. Thus, the $AB'A'^{\downarrow}_{\uparrow}$ stacking adjacent to the hexagonal lattice defects (Fig. 6d) is suggested to be the uncompleted C36 stacking. The change in stacking sequence can apparently be ascribed to the accommodation of lattice strain during CAF. For this special feature, the hexagonal Type II defect, with larger elongated edges and a more highly depleted Zn zone (Fig. 6e), can possibly be recognized as the precursor of a Type I defect. Here, accompanied by the incompatible stackings of $AB'A'^{\downarrow}_{\uparrow}AB'$, the Type II defect, it is assumed, would gradually decompose into a hexagonal Type I defect and a rhombic unit to release the lattice strain during the dynamic interaction of CAF. More work on VASP will be necessary to confirm the evolution of these two types of elongated hexagonal defects.

For the other three HAADF-STEM $(2\bar{1}\bar{1}0)\eta$ images of η_2, η_{13} and η_{14}, shown in Figs. 7–9, the atomic lattice defects introduced during the dynamic precipitation of CAF have also been identified, and their change in the stacking sequences have been evaluated. For η_2 (Fig. 8), the atomic arrays adjacent to the irregular sub-unit defect chain are composed of five distinctive regions, i.e., the uncompleted C36 ($AB'A'^{\downarrow}_{\uparrow}$), C14 (AB'), perfect C36 (AB'A'C), C15 (ABC), and C14 (AB') stackings from the lower left part to the upper right part of the chain as shown in Fig. 8e. The change in stackings can be identified by examinations of the $(2\bar{1}\bar{1}0)\eta_2$ projection rhombic units (Figs. 8d and e) with respect to Komura's rule (Fig. 1c). However, the transformations between the C14, C36 and C15 of

Laves phases are unclear [29, 38, 68, 69]. In an investigation of Cr_2Hf (C14) Laves phases [38], Kumar et al. indicated that the transformations of C14 → C36 and C14 → C15 can be achieved by the glide of dislocations on the (0001) basal plane of C14. In a simulation investigation on the nanoscale deformation of Mg_2Ca (C14) Laves phases [68], Guénolé et al. revealed that the propagation of Shockley partial dislocations accompanies the phase transformation of C14 → C36. However, for η-$MgZn_2$ (C14) Laves phases in Mg-Zn magnesium alloys, Ma et al. [69] pointed out that the $(2\bar{1}\bar{1}0)_\eta$ layered-stackings of C14 change into C15 and then into C36, which can be ascribed to the formations of stacking faults within particles. On the other hand, for η-$MgZn_2$ precipitates in Al-Zn-Mg-Mn aluminium alloys, Yang et al. [29] reported that the phase transformation is to be C14 → C36 → C15 accompanied by stacking faults in the following precipitates. It is appropriate to consider that the compositions and surrounding matrix of Laves phases play a vital role in determining the transformation sequence for C14, C36 and C15 structures. Moreover, it is possible that the different types of η-$MgZn_2$ precipitates in Al-Zn-Mg-Mn aluminium alloys, which grow with different orientations to the aluminium matrix, may induce different lattice strains and further change the transformation sequence. This possibility will need to be elucidated in our future VASP work.

On the other hand, in comparison to the regular zig-zag stacking of η_{13} precipitates subjected to artificial ageing treatment [19], the $(2\bar{1}\bar{1}0)_\eta$ atomic projection of η_{13} in the present work (Fig. 7) shows that CAF may facilitate the irregular sub-unit defect chains (Fig. 7d). Here, the fault unit, A' unit, can be identified to be located between C15 (ABC) and C14 (AB') as shown in Fig. 7e. It is appropriate to suggest that the lattice strain accommodation to neutralize the effect of the dynamic

precipitate could be associated with the incompatible stacking. As for the new type of η_{14} precipitate, the $(2\bar{1}\bar{1}0)\eta$ atomic projection of η_{14} (Fig. 9a) shows that the faulted layers approximately along the $(0002)\eta_{14}$ // $(51\bar{3})_{Al}$ plane pass entirely through the particle. These faulted layers can be identified as embedded in the C36–C14 stackings (Fig. 9d) but are not accompanied by any elongated hexagonal defects.

4.3 Effect of CAF-induced lattice defects on the morphology of η

In Fig. 4, it can be observed that uniform rhombic-stacking η_1 without any different-geometrical lattice defects exhibits the plate-like morphology, where the broader interface of η_1 (Fig. 4a) is parallel to the $(0\bar{2}20)\eta_1$ plane, leading to the elongated diffraction spots (Fig. 4b). In a previous work [28], the plate-like morphology of η_1-$MgZn_2$ precipitates in the Al-Zn-Mg aluminium alloy has been reported. It has also pointed out that the differently-oriented distribution of the elongated hexagonal lattice defects within η_1 can bring about a change in the morphology of this precipitate, resulting in a bulged shape [28]. In the present work, the HAADF-STEM $(2\bar{1}\bar{1}0)$ images of η_1 (Fig. 5a) and η_{12} (Fig. 6a) observed along the zone axis of $[2\bar{1}\bar{1}0]\eta$ reveal a nearly spherical-like morphology unlike the plate-like morphology of η_1 (Fig. 4), η_2 (Fig. 8), η_{13} (Fig. 7) and η_{14} (Fig. 9). The $(2\bar{1}\bar{1}0)$ atomic projections of the nearly-spherical η_1 (Fig. 5) and η_{12} (Fig. 6) clearly display not only the differently-oriented elongated hexagonal defects but also the Penrose tiling features with five-fold symmetry, which exhibit a configuration similar to the icosahedron crystal [67]. It is appropriate to conclude that

the Penrose tiling features presumably affect the growth directions of η_1 and η_{12}, leading to the spherical morphology instead of the typical plate-like morphology.

On the other hand, the effect of the irregular sub-unit defect chain on the change in the morphology of particles is not obvious, as shown in η_2 (Fig. 8) and η_{13} (Fig. 7), which exhibit the plate-like morphology; this morphology is different from the spherical morphology of η_1 (Fig. 5) and η_{12} (Fig. 6). The $(2\bar{1}\bar{1}0)\eta$ atomic projections of η_2 (Fig. 8) and η_{13} (Fig. 7) are characterized by zig-zag stackings with sub-unit defect chains, which incorporate some differently-oriented elongated hexagonal lattice defects but without any Penrose tiling features. Notably, in the cases of η_2 and η_{13} precipitate, the sub-unit defect chains accompanied laterally by several faulted layers, which are interwoven with the regular zig-zag arrays in the matrices of precipitates, have a negligible effect on the morphology of the transformation fronts. For the new type of plate-like η_{14} precipitate (Fig. 9), the $(2\bar{1}\bar{1}0)\eta$ atomic projection shows that the resulting faulted layers nearly along the $(0002)\eta_{14}$ // $(51\bar{3})_{Al}$ plane pass entirely through the precipitate, leading to the formation of the broader $(2\bar{2}04)\eta_{14}$ interface for the lattice strain accommodation. Here, these faulted layers are not accompanied by any elongated hexagonal defects as compared to the observations for η_1 (Fig. 5), η_2 (Fig. 8), η_{12} (Fig. 6) and η_{13} (Fig. 7).

4.4 Effect of CAF on atomic diffusion adjacent to transformation fronts of η

In the previous work [70], it was claimed that in an Al-Zn-Mg-Cu aluminium alloy, the energy-favored Zn segregation occurred adjacent to the broad interface of η' precipitates, according to first-

principles calculations. In the present work, under the $[2\bar{1}\bar{1}0]\eta_{14}$ // $[112]_{Al}$ zone axis the atomic STEM image can reveal the diffusion path of Zn/Cu atoms in the η_{14} precipitate (Fig. 9e), where the $(2\bar{2}04)\eta_{14}$ transformation front is inclined to $(11\bar{1})_{Al}$ plane. Thus, along the zone axis of $[112]_{Al}$, the traces of Zn/Cu atom diffusion in the $<1\bar{1}0>_{Al}$ directions with respect to the $\{11\bar{1}\}_{Al}$ planes can be observed by focusing on the $[1\bar{1}0]_{Al}$ direction of the $(11\bar{1})_{Al}$ plane. Here, under observation along the zone axis of $[112]_{Al}$ // $[2\bar{1}\bar{1}0]\eta_{14}$ (Fig. 9e), the atomic projection $(2\bar{1}\bar{1}0)$ image of η_{14} can clearly reveal the traces of Zn/Cu diffusion along the $(11\bar{1})_{Al}$ planes with the Z-contrast gradient in the $[1\bar{1}0]_{Al}$ directions approaching to the transformation front. However, for η_2 precipitate under the observation along the zone axis of $[112]_{Al}$ // $[2\bar{1}\bar{1}0]\eta_2$ (Fig. 8), the $(0001)\eta_2$ transformation front is determined to be exactly parallel to $(11\bar{1})_{Al}$ plane, therefore the gradient of Z-contrast adjacent to the transformation front cannot be identified due to the edge-on configuration of $(11\bar{1})_{Al}$ planes. For the case of η_{14} (Fig. 9e), given that the sample thickness is assumed to be uniform in this small area, atomic columns adjacent to the transformation front of η_{14} have a higher Z-contrast along the $(11\bar{1})_{Al}$ plane in the aluminium matrix. The corresponding intensity line profiles are provided in Supplementary Fig. 5 in Supplementary Material. The atomic columns with the highest intensity approaching the transformation front of η_{14} precipitates can be related to the segregation of Zn/Cu atoms at the interface, which is presumably facilitated via CAF. Obviously, the Zn/Cu atoms preferentially diffuse along the close-packed $[\bar{1}10]_{Al}$ and $[1\bar{1}0]_{Al}$ directions on the $(11\bar{1})_{Al}$ plane, promoting the growth and coarsening of η. On the other hand, the corresponding atomic concentration gradient for each specific element in the matrix approaching the transformation front of the precipitate should be further

investigated and quantified by atomic energy-dispersive X-ray spectroscopy (EDS) in a future work to provide detailed chemistry analysis information.

5. Conclusions

HAADF STEM has shown that, during the dynamic precipitation of creep-age forming treatment, the interaction between precipitates and dislocations occurs at the impingement between η phases and the tangled dislocations. The atomic lattice defects within η precipitates, created by creep-age forming, have been intensively examined by HR HAADF STEM on atomic projection $(2\bar{1}\bar{1}0)\eta$ configurations of η precipitates. It is revealed that the regular zig-zag stackings of η precipitates are frequently interrupted by the formation of faulted layers and that the sub-unit defect chains incorporating some differently-oriented elongated hexagonal lattice defects occur. A simulated atomic model with the Komura atomic arrays has been used to create the 3-D atomic structures of η, followed by the 2-D atomic stacking constructions for comparison with HR HAADF STEM images. The atomic arrays adjacent to the defect chains in the different types of η precipitates have been examined, and the possible configurations are suggested to be the main frames, C14 Laves structures, interwoven with C15/C36 Laves structures. In η_1, η_2, η_{12} and η_{13} precipitates, two types of elongated hexagonal lattice defects, Type I and Type II defects, can be identified. The Penrose tiling features are also found to be connected with differently-oriented elongated hexagonal Type I lattice defects, leading to the spherical-like morphology of η_1 and η_{12} precipitates. The newly-typed η_{14} precipitate with some entirely-passed stacking faulted layers is identified by a new orientation relationship with respect to

the aluminium matrix: $[112]_{Al}$ // $[2\bar{1}\bar{1}0]\eta_{14}$ and $(51\bar{3})_{Al}$ // $(0001)\eta_{14}$. In the HR HAADF-STEM atomic projection $(2\bar{1}\bar{1}0)$ image of η_{14}, the traces of Zn/Cu diffusion are clearly revealed along the $(11\bar{1})_{Al}$ planes, with the Z-contrast gradient in the $[\bar{1}10]_{Al}$ direction approaching the transformation front.

Acknowledgement:

This work was performed with financial support from the SMART Center of NTU-NIMS and the Ministry of Science and Technology (Taiwan) under Contracts MOST106-2923-E-002009MY2 and MOST108-2622-E-002-016-CC2. The authors are grateful to the Taiwan Instrument Research Institute and Materials Analysis Technology Inc. (MA-tek) for technical advice.

Reference

[1] A. Deschamps, G. Fribourg, Y. Bréchet, J.L. Chemin, C.R. Hutchinson, In situ evaluation of dynamic precipitation during plastic straining of an Al–Zn–Mg–Cu alloy, Acta Mater. 60 (2012) 1905-1916.

[2] C.R. Hutchinson, F. de Geuser, Y. Chen, A. Deschamps, Quantitative measurements of dynamic precipitation during fatigue of an Al–Zn–Mg–(Cu) alloy using small-angle X-ray scattering, Acta Mater. 74 (2014) 96-109.

[3] W. Sun, Y. Zhu, R. Marceau, L. Wang, Q. Zhang, X. Gao, C. Hutchinson, Precipitation strengthening of aluminum alloys by room-temperature cyclic plasticity, Science 363 (2019) 972-975.

[4] L. Zhan, J. Lin, T.A. Dean, A review of the development of creep age forming: Experimentation, modelling and applications, Int. J. Mach. Tools Manuf. 51 (2011) 1-17.

[5] Y. Li, Z. Shi, J. Lin, Y.-L. Yang, B.-M. Huang, T.-F. Chung, J.-R. Yang, Experimental investigation of tension and compression creep-ageing behaviour of AA2050 with different initial tempers, Mater. Sci. Eng. A 657 (2016) 299-308.

[6] Y. Li, Z. Shi, J. Lin, Y.-L. Yang, Q. Rong, B.-M. Huang, T.-F. Chung, C.-S. Tsao, J.-R. Yang, D.S. Balint, A unified constitutive model for asymmetric tension and compression creep-ageing behaviour of naturally aged Al-Cu-Li alloy, Int. J. Plast. 89 (2017) 130-149.

[7] J. Zhang, Y. Wang, Y. Deng, X. Zhang, Effect of deformation degree on the creep age forming of 7475 aluminum alloy: The feasibility of the extended deformation range, Mater. Sci. Eng. A 664 (2016) 126-134.

[8] Y.-L. Yang, A.C. Lam, Z. Shi, J. Lin, R. Said, Constitutive modelling of creep-ageing behaviour of peak-aged aluminium alloy 7050, Matec. Web. Conf., EDP Sciences, 2015.

[9] Y.C. Lin, Y.-Q. Jiang, X.-C. Zhang, J. Deng, X.-M. Chen, Effect of creep-aging processing on corrosion resistance of an Al–Zn–Mg–Cu alloy, Mater. Des. 61 (2014) 228-238.

[10] H. Li, T.-J. Bian, C. Lei, G.-W. Zheng, Y.-F. Wang, Dynamic interplay between dislocations and precipitates in creep aging of an Al-Zn-Mg-Cu alloy, Adv. Manuf. 7 (2019) 15-29.

[11] J.F. Chen, L. Zhen, J.T. Jiang, L. Yang, W.Z. Shao, B.Y. Zhang, Microstructures and mechanical properties of age-formed 7050 aluminum alloy, Mater. Sci. Eng. A 539 (2012) 115-123.

[12] Y. Lin, J.-L. Zhang, M.-S. Chen, Evolution of precipitates during two-stage stress-aging of an Al-Zn-Mg-Cu alloy, J. Alloys Compd. 684 (2016) 177-187.

[13] Y.C. Lin, X.-B. Peng, Y.-Q. Jiang, C.-J. Shuai, Effects of creep-aging parameters on aging precipitates of a two-stage creep-aged Al–Zn–Mg–Cu

alloy under the extra compressive stress, J. Alloys Compd. 743 (2018) 448-455.

[14] R.M. Allen, J.B. VanDer Sande, A high resolution transmission electron microscope study of early stage precipitation on dislocation lines in Al-Zn-Mg, Metall. Trans. A 9 (1978) 1251-1258.

[15] T.-F. Chung, Y.-L. Yang, B.-M. Huang, Z. Shi, J. Lin, T. Ohmura, J.-R. Yang, Transmission electron microscopy investigation of separated nucleation and in-situ nucleation in AA7050 aluminium alloy, Acta Mater. 149 (2018) 377-387.

[16] T.-F. Chung, Y.-L. Yang, M. Shiojiri, C.-N. Hsiao, W.-C. Li, C.-S. Tsao, Z. Shi, J. Lin, J.-R. Yang, An atomic scale structural investigation of nanometre-sized η precipitates in the 7050 aluminium alloy, Acta Mater. 174 (2019) 351-368.

[17] H. Degischer, W. Lacom, A. Zahra, C. Zahra, Decomposition Processes in an Al--5% Zn--1% Mg Alloy. II.--Electromicroscopic Investigation, Zeitschrift fur Metallkunde 71 (1980) 231-238.

[18] S. Ringer, K. Hono, Microstructural evolution and age hardening in aluminium alloys: Atom probe field-ion microscopy and transmission electron microscopy studies, Mater. Charact. 44 (2000) 101-131.

[19] A. Bendo, K. Matsuda, A. Lervik, T. Tsuru, K. Nishimura, N. Nunomura, R. Holmestad, C.D. Marioara, K. Shimizu, H. Toda, An unreported precipitate orientation relationship in Al-Zn-Mg based alloys, Mater. Charact. 158 (2019) 109958.

[20] J.B. Friauf, The Crystal Structure of Magnesium Di-Zincide, Phys. Rev. 29 (1927) 34-40.

[21] Y. Komura, Stacking faults and two new modifications of the Laves phase in Mg–Cu–Al system, Acta Crystallogr. 15 (1962) 770-778.

[22] F.t. Frank, J. Kasper, Complex alloy structures regarded as sphere packings. II. Analysis and classification of representative structures, Acta Crystallogr. 12 (1959) 483-499.

[23] Y. Komura, E. Kishida, M. Inoue, The Crystal Structure of the Laves Phase in Mg-Zn-Ag-System. I, J. Phys. Soc. Jpn. 23 (1967) 398-404.

[24] A. Bendo, K. Matsuda, S. Lee, K. Nishimura, N. Nunomura, H. Toda, M. Yamaguchi, T. Tsuru, K. Hirayama, K. Shimizu, H. Gao, K. Ebihara, M. Itakura, T. Yoshida, S. Murakami, Atomic scale HAADF-STEM study of η' and η_1 phases in peak-aged Al–Zn–Mg alloys, J. Mater. Sci. 53 (2018) 4598-4611.

[25] C.D. Marioara, W. Lefebvre, S.J. Andersen, J. Friis, Atomic structure of hardening precipitates in an Al–Mg–Zn–Cu alloy determined by HAADF-STEM and first-principles calculations: relation to η-$MgZn_2$, J. Mater. Sci. 48 (2013) 3638-3651.

[26] X. Xu, J. Zheng, Z. Li, R. Luo, B. Chen, Precipitation in an Al-Zn-Mg-Cu alloy during isothermal aging: Atomic-scale HAADF-STEM investigation, Mater. Sci. Eng. A 691 (2017) 60-70.

[27] S.J. Andersen, C.D. Marioara, J. Friis, S. Wenner, R. Holmestad, Precipitates in aluminium alloys, Adv. Phys.: X 3 (2018) 790-813.

[28] A. Bendo, T. Maeda, K. Matsuda, A. Lervik, R. Holmestad, C.D. Marioara, K. Nishimura, N. Nunomura, H. Toda, M. Yamaguchi, Characterisation of structural similarities of precipitates in Mg–Zn and Al–Zn–Mg alloys systems, Philos. Mag. 99 (2019) 2619-2635.

[29] T. Yang, Y. Kong, J. Lu, Z. Zhang, M. Yang, N. Yan, K. Li, Y. Du, Self-accommodated defect structures modifying the growth of Laves phase, Journal of Materials Science & Technology 62 (2020) 203-213.

[30] J.M. Rosalie, H. Somekawa, A. Singh, T. Mukai, Orientation relationships between icosahedral clusters in hexagonal $MgZn_2$ and monoclinic Mg_4Zn_7 phases in Mg-Zn(-Y) alloys, Philos. Mag. 91 (2011) 2634-2644.

[31] J.M. Rosalie, H. Somekawa, A. Singh, T. Mukai, Structural relationships among $MgZn_2$ and Mg_4Zn_7 phases and transition structures in Mg-Zn-Y alloys, Philos. Mag. 90 (2010) 3355-3374.

[32] R. Berry, G.V. Raynor, The crystal chemistry of the Laves phases, Acta Crystallogr. 6 (1953) 178-186.

[33] Y. Komura, K. Tokunaga, Structural studies of stacking variants in Mg-base Friauf–Laves phases, Acta Crystallogr., Sect. B: Struct. Crystallogr. Cryst. Chem. 36 (1980) 1548-1554.

[34] Y. Kitano, Y. Komura, H. Kajiwara, E. Watanabe, Two-dimensional lattice image of the Mg-base Friauf–Laves phase and a new type of defect, Acta Crystallogr., Sect. A: Cryst. Phys., Diffr., Theor. Gen. Crystallogr. 36 (1980) 16-21.

[35] Y. Kitano, Y. Komura, H. Kajiwara, Electron microscope observation of Friauf-Laves phase Mg $(Cu_{1-x}Al_x)_2$ with x= 0.465, Trans. Jpn. Inst. Met 18 (1977) 39-45.

[36] M.D. Graef, M.E. McHenry, Metallic structures ll: complex geometrically determined structures, Structure of Materials: An Introduction to Crystallography, Diffraction and Symmetry, Cambridge University Press2012, pp. 466-496.

[37] P.M. Hazzledine, P. Pirouz, Synchroshear transformations in Laves phases, Scr. Metall. Mater. 28 (1993) 1277-1282.

[38] K.S. Kumar, P.M. Hazzledine, Polytypic transformations in Laves phases, Intermetallics 12 (2004) 763-770.

[39] F. Stein, M. Palm, G. Sauthoff, Structure and stability of Laves phases. Part I. Critical assessment of factors controlling Laves phase stability, Intermetallics 12 (2004) 713-720.

[40] B.S. Murty, J.-W. Yeh, S. Ranganathan, P.P. Bhattacharjee, Special subgroups of high-entropy alloys, in: B.S. Murty, J.-W. Yeh, S. Ranganathan, P.P. Bhattacharjee (Eds.), High-Entropy Alloys, Elsevier2019, pp. 145-164.

[41] G. Kresse, J. Furthmüller, Efficient iterative schemes for ab initio total-energy calculations using a plane-wave basis set, Phys. Rev. B 54 (1996) 11169-11186.

[42] G. Kresse, D. Joubert, From ultrasoft pseudopotentials to the projector augmented-wave method, Phys. Rev. B 59 (1999) 1758-1775.

[43] C. Wolverton, Crystal structure and stability of complex precipitate phases in Al–Cu–Mg–(Si) and Al–Zn–Mg alloys, Acta Mater. 49 (2001) 3129-3142.

[44] J. Gjønnes, C.J. Simensen, An electron microscope investigation of the microstructure in an aluminium-zinc-magnesium alloy, Acta Metall. 18 (1970) 881-890.

[45] P. Auger, J. Raynal, M. Bernole, R. Graf, X-Ray and Electron-Microscopy Study of Precipitation in Al-Zn-Mg and Al-Zn-Mg-Cu Alloys Tempered Between 100 and 300 C, Mem. Sci. Rev. Met. 71 (1974) 557-568.

[46] G. Sha, Y.B. Wang, X.Z. Liao, Z.C. Duan, S.P. Ringer, T.G. Langdon, Influence of equal-channel angular pressing on precipitation in an Al–Zn–Mg–Cu alloy, Acta Mater. 57 (2009) 3123-3132.

[47] P.A. TRACERY, The nature and morphology of precipitate in AL-Zn-Mg alloys, J. Inst. Met. 961860 (1968) 228-235.

[48] W. Yang, S. Ji, M. Wang, Z. Li, Precipitation behaviour of Al–Zn–Mg–Cu alloy and diffraction analysis from η' precipitates in four variants, J. Alloys Compd. 610 (2014) 623-629.

[49] X.Z. Li, V. Hansen, J. GjØnnes, L.R. Wallenberg, HREM study and structure modeling of the η' phase, the hardening precipitates in commercial Al–Zn–Mg alloys, Acta Mater. 47 (1999) 2651-2659.

[50] H. Löffler, I. Kovacs, J. Lendvai, Decomposition processes in Al-Zn-Mg alloys, J. Mater. Sci. 18 (1983) 2215-2240.

[51] D. Godard, P. Archambault, E. Aeby-Gautier, G. Lapasset, Precipitation sequences during quenching of the AA 7010 alloy, Acta Mater. 50 (2002) 2319-2329.

[52] A. Lervik, C.D. Marioara, M. Kadanik, J.C. Walmsley, B. Milkereit, R. Holmestad, Precipitation in an extruded AA7003 aluminium alloy: Observations of 6xxx-type hardening phases, Mater. Des. 186 (2020) 108204.

[53] H. Schmalzried, V. Gerold, Age-hardening in an Al-Mg-Zn alloy, Zeitschrift für Metallkunde 49 (1958) 291-301.

[54] M. Dumont, W. Lefebvre, B. Doisneau-Cottignies, A. Deschamps, Characterisation of the composition and volume fraction of η' and η precipitates in an Al–Zn–Mg alloy by a combination of atom probe, small-angle X-ray scattering and transmission electron microscopy, Acta Mater. 53 (2005) 2881-2892.

[55] J.C. Werenskiold, A. Deschamps, Y. Bréchet, Characterization and modeling of precipitation kinetics in an Al–Zn–Mg alloy, Mater. Sci. Eng. A 293 (2000) 267-274.

[56] B. Cheng, X. Zhao, Y. Zhang, H. Chen, I. Polmear, J.-F. Nie, Co-segregation of Mg and Zn atoms at the planar η_1-precipitate/Al matrix interface in an aged Al–Zn–Mg alloy, Scripta Mater. 185 (2020) 51-55.

[57] J.D. Embury, R.B. Nicholson, The nucleation of precipitates: The system Al-Zn-Mg, Acta Metall. 13 (1965) 403-417.

[58] M. Shiojiri, H. Saijo, Imaging of high-angle annular dark-field scanning transmission electron microscopy and observations of GaN-based violet laser diodes, Journal of microscopy 223 (2006) 172-178.

[59] C. Lei, H. Li, J. Fu, T.J. Bian, G.W. Zheng, Non-isothermal creep aging behaviors of an Al-Zn-Mg-Cu alloy, Mater. Charact. 144 (2018) 431-439.

[60] K. Ma, H. Wen, T. Hu, T.D. Topping, D. Isheim, D.N. Seidman, E.J. Lavernia, J.M. Schoenung, Mechanical behavior and strengthening mechanisms in ultrafine grain precipitation-strengthened aluminum alloy, Acta Mater. 62 (2014) 141-155.

[61] A. Singh, J.M. Rosalie, Lattice Correspondence and Growth Structures of Monoclinic Mg_4Zn_7 Phase Growing on an Icosahedral Quasicrystal, Crystals 8 (2018) 194.

[62] Y.-P. Xie, Z.-Y. Wang, Z.F. Hou, The phase stability and elastic properties of $MgZn_2$ and Mg_4Zn_7 in Mg–Zn alloys, Scripta Mater. 68 (2013) 495-498.

[63] A. Singh, Tailoring microstructure of Mg–Zn–Y alloys with quasicrystal and related phases for high mechanical strength, Sci. Technol. Adv. Mater. 15 (2014) 044803-p1-p16.

[64] M. De Graef, Electron diffraction patterns, Introduction to conventional transmission electron microscopy, Cambridge University, Pennsylvania, 2003, pp. 518-584.

[65] X. Fang, M. Song, K. Li, Y. Du, D. Zhao, C. Jiang, H. Zhang, Effects of Cu and Al on the crystal structure and composition of η ($MgZn_2$) phase in over-aged Al–Zn–Mg–Cu alloys, J. Mater. Sci. 47 (2012) 5419-5427.

[66] J.K. Sunde, D.N. Johnstone, S. Wenner, A.T.J. van Helvoort, P.A. Midgley, R. Holmestad, Crystallographic relationships of T-/S-phase aggregates in an Al–Cu–Mg–Ag alloy, Acta Mater. 166 (2019) 587-596.

[67] Z. Shen, C. Liu, Q. Ding, S. Wang, X. Wei, L. Chen, J. Li, Z. Zhang, The structure determination of $Al_{20}Cu_2Mn_3$ by near atomic resolution chemical mapping, J. Alloys Compd. 601 (2014) 25-30.

[68] J. Guénolé, F.-Z. Mouhib, L. Huber, B. Grabowski, S. Korte-Kerzel, Basal slip in Laves phases: The synchroshear dislocation, Scripta Mater. 166 (2019) 134-138.

[69] L. Ma, T.-W. Fan, B.-Y. Tang, L.-M. Peng, W.-j. Ding, Ab initio study of I_2 and T_2 stacking faults in C14 Laves phase $MgZn_2$, The European Physical Journal B 86 (2013) 188.

[70] F. Cao, J. Zheng, Y. Jiang, B. Chen, Y. Wang, T. Hu, Experimental and DFT characterization of η' nano-phase and its interfaces in Al-Zn-Mg-Cu alloys, Acta Mater. 164 (2019) 207-219.